nature immunology

Article

https://doi.org/10.1038/s41590-026-02435-4

Piezo1-dependent activation of stromal cells ignites muscle inflammation in exercise and injury and is associated with inflammaging

Received: 19 May 2025

Accepted: 14 January 2026

Published online: 3 March 2026

Check for updates

P. Kent Langston[1,2], Jayashree Vijaya Raghavan[1,3], Christophe Benoist[1] & Diane Mathis[1]

As the actuator of movement and a key regulator of organismal metabolism, skeletal muscle is a site at which inflammatory responses must be carefully calibrated to counteract stressors while preventing protracted functional impairments. Exercise, injury and aging are common forms of stress associated with inflammation; yet the specific inducers and sensors driving such inflammation remain poorly characterized. Multipronged assessment of acute and chronic endurance exercise models uncovered a role for muscle mesenchymal stromal cells in transducing exercise-induced mechanical stress into local inflammatory responses and that the mechanosensitive ion channel Piezo1 is the primary molecular sensor. Mechanosensing by stromal cells is also necessary for appropriately timed inflammatory and myogenic responses to acute muscle injury and is associated with age-related muscle inflammation. These findings highlight sensing of altered tissue stiffness by Piezo1 on muscle mesenchymal stromal cells as a fundamental mechanism of stress-induced immunomodulation in skeletal muscle.

Physical inactivity increases the risk of developing one or more of the many modern afflictions associated with chronic low-grade inflammation, including cardiovascular disease, cancer and type 2 diabetes[1]. Simply meeting the minimum level of leisure time physical activity recommended by the US Department of Health and Human Services reduces one's risk of mortality from all causes by 27%; greater levels of physical activity, up to tenfold over the minimum, magnify this effect[2]. Until recently, efforts to uncover mechanisms underlying the salubrious effects of physical activity and exercise (intentional physical activity) have primarily focused on parenchymal cells. Although such studies have been fruitful, including the large-scale National Institutes of Health-funded initiative led by the Molecular Transducers of Physical Activity Consortium to generate an organism-wide multiomic map of exercise adaptations[3,4], they do not sufficiently capture the multicellular nature of tissue responses to stress. It is important to address this layer of complexity as it is increasingly apparent that nonparenchymal cells, including immunocytes and mesenchymal stromal cells (mSCs), also respond to exercise and adopt functional states calibrated to support adaptation[5–14]. Yet, relatively little is known about the nature and molecular targets of the exercise-induced signals that call these nonparenchymal, or support-type, cells into action.

Inflammatory responses to physiological and pathological stress are somewhat overlapping, particularly in skeletal muscle[6]. Therefore, we wondered whether the stress-associated signals and their cellular and molecular sensors might also be conserved. In a recent time-resolved single-cell RNA-sequencing (RNA-seq) analysis of acutely injured muscles, we identified an 'early-responder' subtype of mSCs. Like the muscle compartment commonly referred to as fibroadipogenic precursors, mSCs are defined by lack of expression of CD45 and CD31 and expression of SCA1 and PDGFRα[15–18]. The early-responder subtype is characterized by high expression of genes encoding an array of immunomodulatory factors, including interleukin-6 (IL-6), IL-33, CCL2,

[1]Department of Immunology, Harvard Medical School, Boston, MA, USA. [2]Present address: Department of Pathology, Yale Center for Research on Aging, Yale School of Medicine, New Haven, CT, USA. [3]Present address: Division of Immunology, Boston Children's Hospital, Harvard Medical School, Boston, MA, USA. e-mail: dm@hms.harvard.edu

CXCL1 and CXCL5 (ref. 19). Depletion of CXCL5 early after cardiotoxin (CTX)-induced injury stunts the initial, rapid recruitment of neutrophils into hindlimb muscle and delays the transition from proinflammatory to prorepair processes, resulting in poor regeneration[19]. There is mounting evidence that endurance exercise also alters the numbers and functional profiles of muscle mSCs (MmSCs)[10,13,20,21]. Notably, using a Cre-driven biotinylation system to generate an organism-wide, cell-type-specific map of exercise-responsive secreted proteins in mice, Wei and colleagues found that, of the 21 cell types surveyed, mSCs were the most perturbed by exercise training (EXT)[11].

Multipronged assessment of acute and chronic endurance exercise models, toxin-induced muscle injury and natural aging revealed that mSCs initiated muscle inflammation at sites of altered environmental stiffness. In contexts of acute exercise and injury, Piezo1 on mSCs was necessary for their activation and consequent inflammatory responses. These findings highlight the Piezo1–MmSC pair as a fundamental mechanism of stress-induced immunomodulation in skeletal muscle.

Results

Acute or chronic endurance exercise induces an inflammatory reaction by muscle stromal cells

To investigate the potential of acute endurance exercise (AEX) to modulate the mSC compartment in skeletal muscle, we subjected sedentary 8- to 10-week-old C57BL/6J mice to a 90-min bout of moderate-intensity running on a motorized treadmill after 2 days of acclimation and performed a cytofluorometric analysis of MmSCs (PDGFRα$^+$SCA1$^+$CD31$^-$CD45$^-$ cells) on day 1 after AEX (Fig. 1a,b and Extended Data Fig. 1a). We previously reported that this model induces a rapid accumulation of immunocytes (CD45$^+$ cells) in muscles (many cell types, including Ly6C^{hi} macrophages (CD64$^+$Ly6G$^-$CD11b$^+$ cells; MFs) and Foxp3$^+$CD4$^+$ regulatory T (T_{reg}) cells, peak on day 1)[5]. Cytofluorometric analysis of pooled hindlimb muscles (the tibialis anterior (TA), gastrocnemius (Ga), soleus (Sol) and quadriceps (Qd) muscles) from sedentary and acutely exercised mice also revealed a significant increase in the total number of MmSCs (Fig. 1b).

We next captured the molecular profiles of MmSCs from these conditions by population-level RNA-seq after cell sorting (Fig. 1c). Pathway analysis of the genes significantly modulated by AEX ($P_{adj} < 0.05$, | fold change (FC) | > 2) revealed a strong upregulation of genes associated with biosynthetic processes (for example, carboxylic acids, amino acids and extracellular matrix (ECM)) and inflammation (Fig. 1d). The transcript most enriched in MmSCs 1 day after AEX was *Tnc* (Fig. 1c), which encodes tenascin-C (TNC), an ECM glycoprotein induced in the mSCs of many tissues by injury[22,23]. TNC is primarily known for its antiadhesion effects, which are mediated by interfering with fibronectin binding, but it is also an endogenous ligand for Toll-like receptor 4 (refs. 24–26). Other AEX-induced transcripts encoding other notable ECM-associated factors included *Ccn4*, which encodes WISP1, a matricellular protein that is required for muscle satellite cell expansion and myogenesis[27], *Postn* (periostin) and *Timp1* (tissue inhibitor of metalloproteinase-1; Fig. 1c). Related to inflammatory processes, enriched transcripts included those specifying F2RL1 (protease-activated receptor 2) and the chemokines CCL2 and CCL7 (Fig. 1c). Enrichment of chemokine gene transcripts is consistent with previous tissue-level transcriptomic analyses of skeletal muscle from exercised versus sedentary mice and humans[28,29].

Many of the genes induced by AEX were reminiscent of those constituting the 'early-responder' inflammatory subtype of MmSCs that we identified in a previous single-cell RNA-seq analysis of injured muscle. Overlay of the corresponding inflammatory stromal cell signature[19] onto a comparison of the transcriptomes of MmSCs from exercised and sedentary mice showed clear enrichment in the former (Fig. 1e). Cytofluorometric analysis of key molecules from this signature revealed a small population of inflammatory stromal cells in hindlimb muscles from sedentary mice that expanded several fold after AEX (Fig. 1f and Extended Data Fig. 1b).

Similar to acute exercise, long-term training promotes accrual of total immunocytes in hindlimb muscles, with a peak at 2 weeks (ref. 5). As per our previous study, we modeled EXT by individually housing mice with unrestricted access to a running wheel for 2 weeks and performed cytofluorometric and transcriptomic analyses after a washout period of 24 h (Fig. 1g–l). EXT also significantly increased the number of mSCs in muscle, and such accrual was proportional to the distance mice ran during training (Fig. 1h,i). Based on cytofluorometric quantification of TNC and ICAM1 expression, 2 weeks of EXT increased the proportions and numbers of inflammatory MmSCs compared to sedentary controls (Fig. 1j and Extended Data Fig. 1c). For additional insight into the molecular changes induced by EXT, we performed population-level RNA-seq on total mSCs from hindlimb muscles of EXT versus sedentary mice. There were fewer genes differentially expressed after EXT than after AEX; however, there was a similar enrichment in transcripts belonging to the inflammatory stromal cell signature (Fig. 1k,l). Of particular interest were *Cxcl5*, which we previously showed to be stroma specific, highly upregulated with injury and critical for neutrophil recruitment to injured muscle[19]; *H19*, which was captured in our whole-muscle transcriptomic assessment of EXT[5] and was previously highlighted in an analysis of data from the HERITAGE Family Study as part of a signature predictive of the response to EXT[30]; and *Bdnf*, encoding brain-derived neurotrophic factor, an exercise-stimulated cytokine (or 'exerkine') implicated in synaptic plasticity, learning and memory[31,32] (Fig. 1k,l).

The exercise-induced inflammatory reaction of MmSCs is localized to mechanically stressed hindlimb muscles

Muscles at different sites experience differing levels of mechanical and metabolic stress during endurance exercise. Our previous study

Fig. 1 | Exercise-induced activation of stromal cells is reminiscent of that induced by injury. a–e, Eight- to 10-week-old mice were acclimated to a motorized treadmill for 2 days and were then made to perform an acute, moderate-intensity bout of endurance exercise. Cytofluorometric ($n \geq 5$) and transcriptomic ($n = 3$) analyses were performed after 24 h of recovery. **a**, Schema for AEX experiments; Acclim., acclimation. **b**, Representative flow cytometric plots of MmSCs before and 24 h after AEX. Numbers beside the gates indicate frequencies of gated cells among CD31$^-$CD45$^-$ cells. Summary numbers per gram of muscle are shown to the right; d1, day 1; SED, sedentary. **c**, RNA-seq analysis of MmSCs sorted from pooled hindlimb muscles (TA, Ga and Qd) from mice 1 day after AEX versus sedentary controls. Differentially expressed genes (adjusted *P* value (P_{adj}) < 0.05, | FC | ≥ 2) are highlighted; genes of high interest are annotated. **d**, Pathway enrichment analysis of differentially expressed genes highlighted in **c**. **e**, Volcano plot overlaid with genes differentially enriched in the early-responder, inflammatory subtype of mSCs found in acutely injured muscle[19]. **f**, Representative flow cytometric plots of TNC$^+$ MmSCs before and 24 h after AEX. Numbers beside the gates indicate frequencies of gated cells among total MmSCs. Summary frequencies and numbers per gram of muscle are shown to the right. **g–l**, Eight-week-old mice were individually housed for 2 weeks with or without unrestricted access to running wheels equipped with activity-tracking software. Hindlimb muscles were isolated for cytofluorometric ($n \geq 5$) and transcriptomic ($n = 3$) analyses after a 24-h washout period. **g**, Schema for EXT experiments. **h**, Number of MmSCs per gram of muscle. **i**, Correlation between voluntary running distance during EXT and number of MmSCs per gram of muscle. **j**, Frequency and number of TNC$^+$ MmSCs per gram of muscle. **k**, RNA-seq analysis of MmSCs sorted from pooled hindlimb muscles (TA, Ga and Qd) from mice 24 h after EXT versus sedentary controls. Differentially expressed genes ($P_{adj} < 0.05$, | FC | ≥ 2) are highlighted; genes of high interest are annotated. **l**, Volcano plot overlaid with genes differentially enriched in the early-responder, inflammatory subtype of mSCs found in acutely injured muscle[19]. Summary plots show data pooled from two or more independent experiments; $^*P < 0.05$, $^{**}P < 0.01$ and $^{****}P < 0.0001$ by an unpaired two-tailed Student's *t*-test (**b**, **f**, **h** and **j**), a simple linear regression (**i**) or Fisher's exact test (**e** and **l**).

https://doi.org/10.1038/s41590-026-02435-4

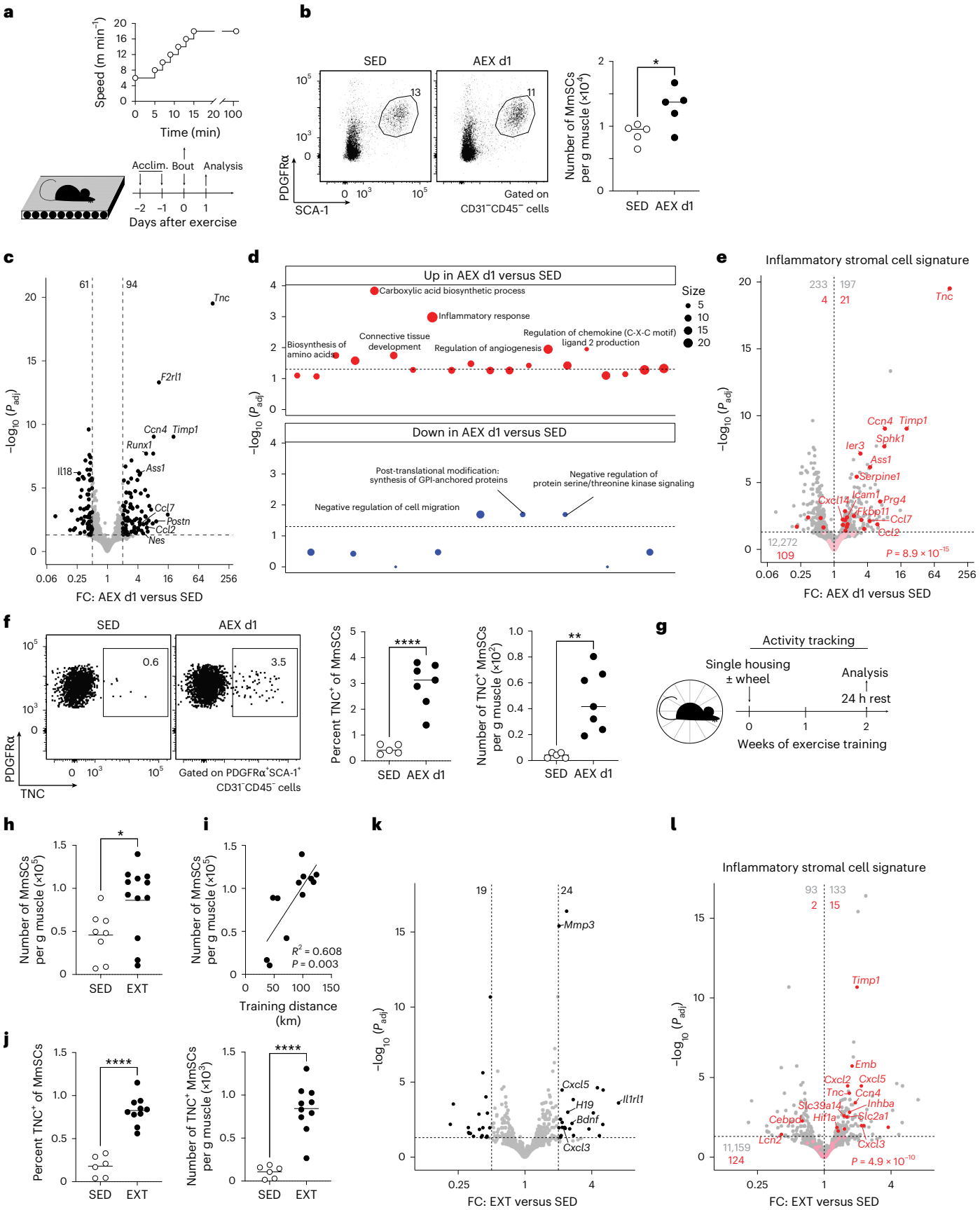

https://doi.org/10.1038/s41590-026-02435-4

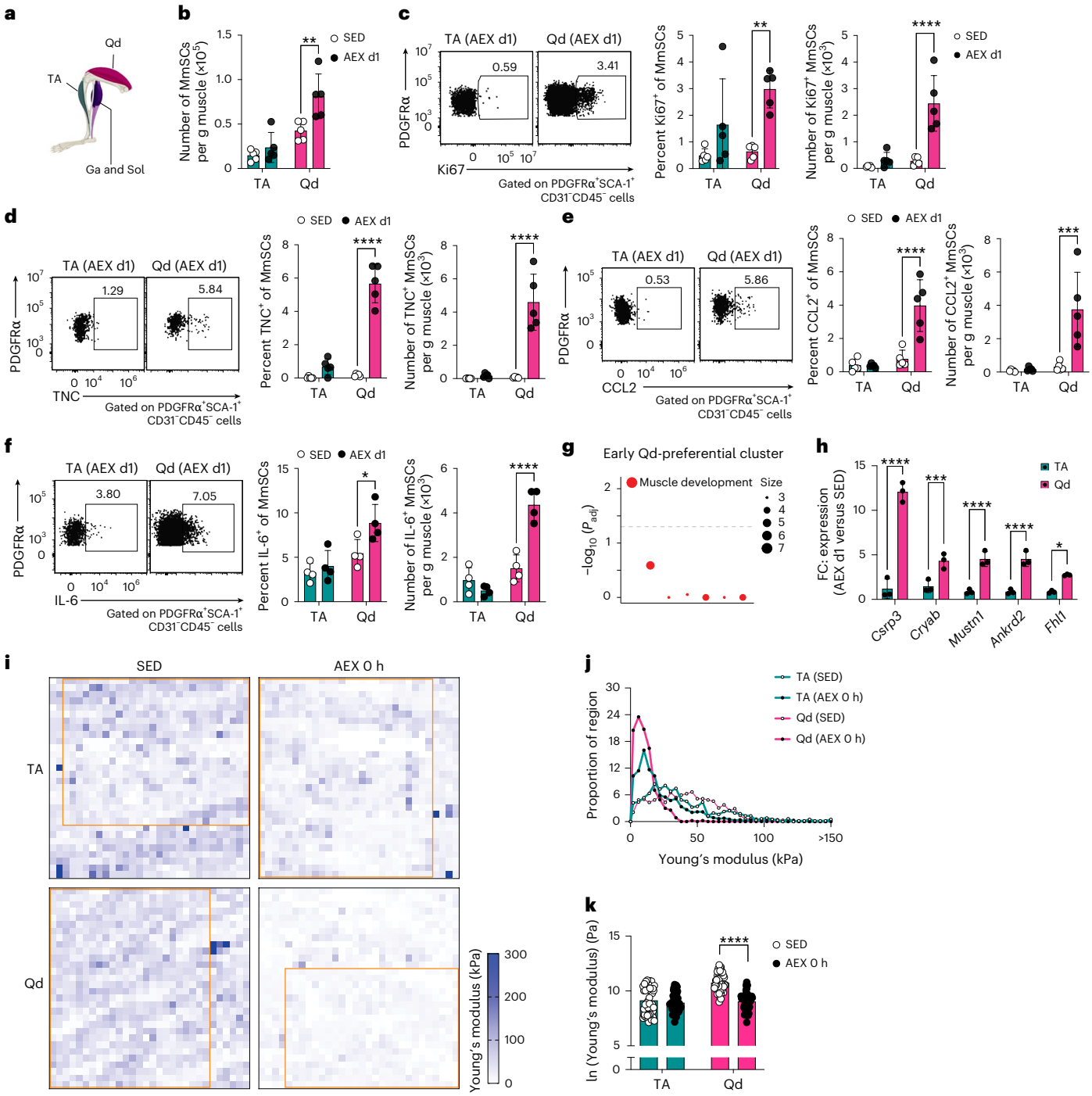

Fig. 2 | Inflammatory activation of MmSCs is site specific and associated with mechanical stress. a, Anatomical map of mouse hindlimb muscles. **b**–**h**, Cytofluorometric ($n \geq 4$) and transcriptomic ($n = 3$) analysis of specific hindlimb muscles from sedentary mice or from mice on day 1 of recovery after AEX. **b**, Number of MmSCs per gram of muscle. **c**–**f**, Representative flow cytometric plots of Ki67$^+$ (**c**), TNC$^+$ (**d**), CCL2$^+$ (**e**) and IL-6$^+$ (**f**) MmSCs in TA muscle versus Qd muscle 24 h after AEX. Numbers beside the gates indicate frequencies of gated cells among total MmSCs. Summary frequencies and numbers per gram of muscle are shown to the right. **g**, Pathway enrichment analysis of genes preferentially induced in Qd versus TA early after AEX, identified previously[5]. **h**, FC in expression of the top five factors in the early Qd-preferential cluster of genes. **i**–**k**, Measurement of tissue stiffness (Young's modulus) by AFM on sections of TA and Qd muscles isolated from mice at rest (SED) or immediately after acute exercise (AEX 0 h). Four mice were used per condition ($n = 4$), and a minimum of three regions were scanned from four sections per muscle (two superficial and two deep). **i**, Representative heat maps showing Young's moduli of TA and Qd muscles before and immediately after AEX. Each region is from a leveled area of 100 µm × 100 µm. Boxed subregions highlight areas selected to avoid topographical errors. **j**, Histograms of Young's modulus values from selected subregions in **i**. **k**, Summary of Young's moduli of TA and Qd muscles before and immediately after AEX. Data points are natural log transformed and represent average Young's modulus per region from three or more regions × four sections × four mice per group. Bar plots are drawn to show geometric means. Summary plots show data pooled from two or more independent experiments. Error bars (**c**–**f** and **h**) represent standard deviation; $^*P < 0.05$, $^{**}P < 0.01$, $^{***}P < 0.001$ and $^{****}P < 0.0001$ by two-way analysis of variance (ANOVA) with Šídák's multiple comparisons test (**b**–**f** and **h**) or unpaired two-tailed *t*-test with Welch's correction (**k**). Panel **a** reproduced with permission from ref. 5, AAAS.

https://doi.org/10.1038/s41590-026-02435-4

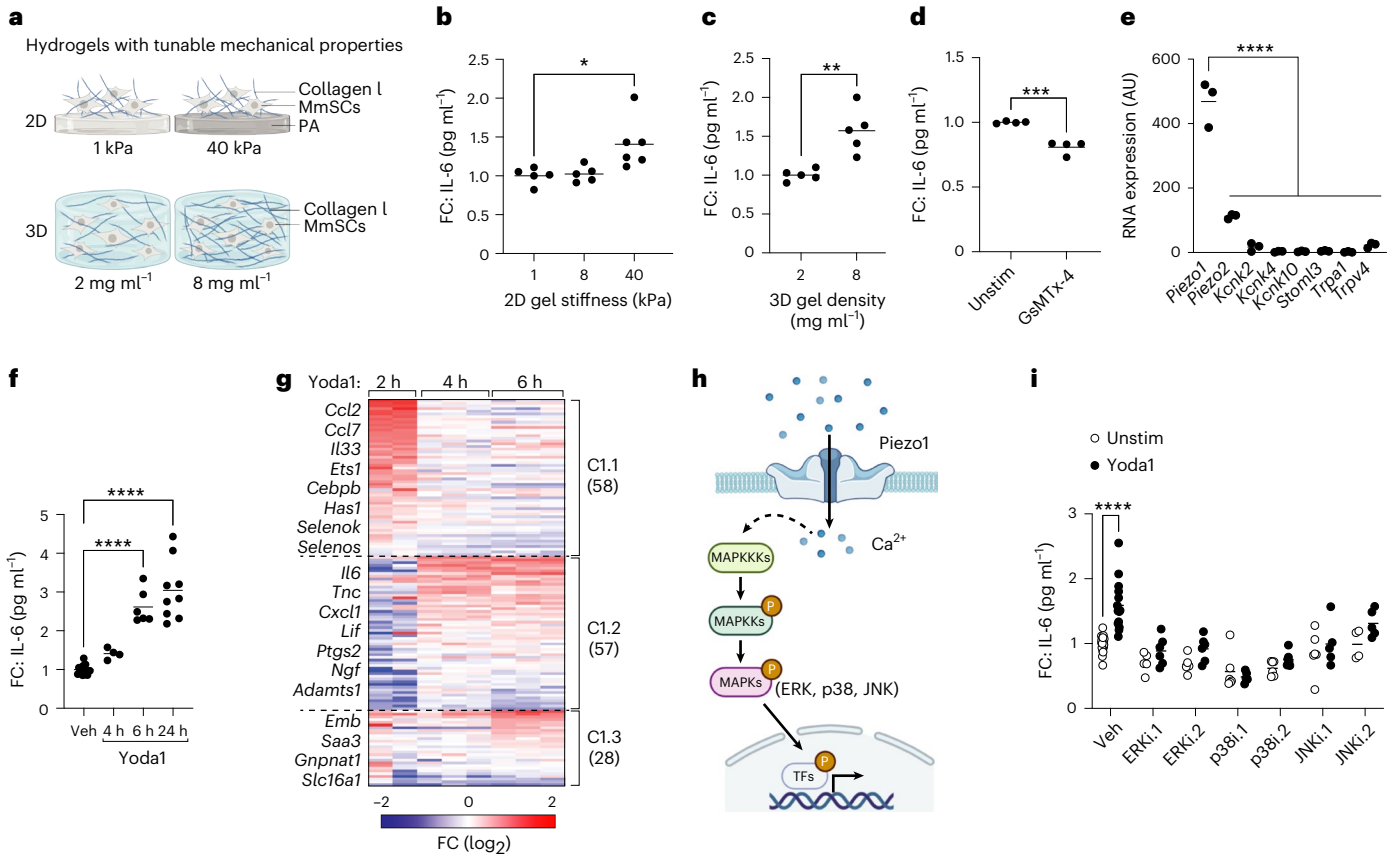

Fig. 3 | Environmentally and chemically induced mechanical stress incite inflammatory activation of MmSCs. a, Depiction of 2D and 3D hydrogels of different mechanical properties. **b**–**d**, IL-6 production by MmSCs after 24 h of culture ($n \geq 4$) on 2D PA-based gels of the indicated stiffness (**b**), culture in 3D collagen-based gels of the indicated density (**c**) and treatment with GsMTx-4 (**d**); Unstim, unstimulated. **e**, Expression (bulk RNA-seq) of stretch-activated ion channels in MmSCs cultured on standard tissue culture plates ($n = 3$); AU, arbitrary units. **f**, IL-6 production by MmSCs over a time course after stimulation via the Piezo1 agonist Yoda1 ($n \geq 4$); Veh, vehicle. **g**, *k*-Means clustering of genes constituting the inflammatory stromal cell signature[19]. Numbers in parentheses indicate the number of genes within each cluster. FC compared to vehicle-treated controls is shown ($n \geq 2$). **h**, Pathway diagram representing potential targets downstream of Piezo1 activation; TFs, transcription factors. **i**, IL-6 production by MmSCs treated with Yoda1 or vehicle for 5 h after 1 h of pretreatment with inhibitors of ERK (ERKi), p38 MAPK (p38i) or JNK (JNKi) compared to vehicle ($n \geq 4$; see text for names and concentrations of compounds). Summary plots show data pooled from two or more independent experiments; $^{*}P < 0.05$, $^{**}P < 0.01$, $^{***}P < 0.001$ and $^{****}P < 0.0001$ by a one-way ANOVA with Dunnett's multiple comparisons test (**b**, **e** and **f**), a two-way ANOVA with Šídák's multiple comparisons test (**i**) or an unpaired two-tailed Student's *t*-test (**c** and **d**). Panels created in BioRender: **a**, Langston, K. https://biorender.com/bn3anht (2026); Langston, K. https://biorender.com/mtsqe4q (2026); **h**, Langston, K. https://biorender.com/4jwve74 (2026).

revealed AEX-induced enrichment of total immunocytes, MFs, Ly6C^{hi} MFs, T_{reg} cells and neutrophils (Ly6G^{+}CD11b^{+}) in Ga/Sol and Qd, but not TA, muscle[5]. We wondered whether the accrual and inflammatory response of MmSCs would map to the same sites. Indeed, cytofluorometric analysis of the prototypes of immunologically inactive (TA) and active (Qd) muscles revealed increased numbers of MmSCs only in the latter case (Fig. 2a,b). Increased proportions and numbers of MmSCs entering the cell cycle 1 day after AEX were also biased toward Qd muscles (Fig. 2c); proliferation measured by EdU incorporation showed the same pattern (Extended Data Fig. 2a). To quantify the inflammatory reaction of MmSCs, we stained for intracellular TNC, CCL2 and IL-6, the prototypical 'myokine'. The fraction and number of stromal cells producing these factors were preferentially augmented in Qd muscles (Fig. 2d–f).

To ascertain why the MmSC population was preferentially activated and expanded in Qd compared to TA muscle, we revisited published tissue-level transcriptomes at these sites over a time course of recovery after AEX[5]. Our original analysis revealed similar shifts in metabolic profiles in the two muscle groups[5], but we see now that there was also preferential enrichment of transcripts encoding factors involved in muscle structure and response to wound healing (*Ankrd2*, *Cryab*, *Mustn1*, *Ankrd2* and *Fhl1*) in Qd early during recovery (Fig. 2g,h), suggesting a higher level of mechanical perturbation. mSCs are exquisitely sensitive to the mechanical properties of their niche[33], and TNC is a long-known stretch-activated factor in stroma[34,35]. Hence, we measured the stiffness of TA and Qd muscles isolated from mice before or immediately after AEX (Fig. 2i–k and Extended Data Fig. 2b,c). Although Qd muscles were stiffer than TA muscles in sedentary mice, with mean Young's moduli of 46.77 and 9.34 kPa, respectively, AEX had a more pronounced softening effect on the former (8.47 kPa; Δ of −38.3 kPa) than on the latter (7.57 kPa; Δ of −1.77 kPa) muscles (Fig. 2k). Thus, the accumulation and inflammatory reaction of stromal cells after exercise map preferentially to muscles that show large changes in mechanical properties.

Niche stiffness and chemical activation of Piezo1 rapidly polarize MmSCs to an immunomodulatory state

Although our dissection of exercise responses showed that the pattern of MmSC activation and inflammation across different hindlimb muscles correlated with tissue-level transcriptional and biomechanical changes indicative of mechanical stress, there are other signals, such as damage-associated molecular patterns, that logically would

https://doi.org/10.1038/s41590-026-02435-4

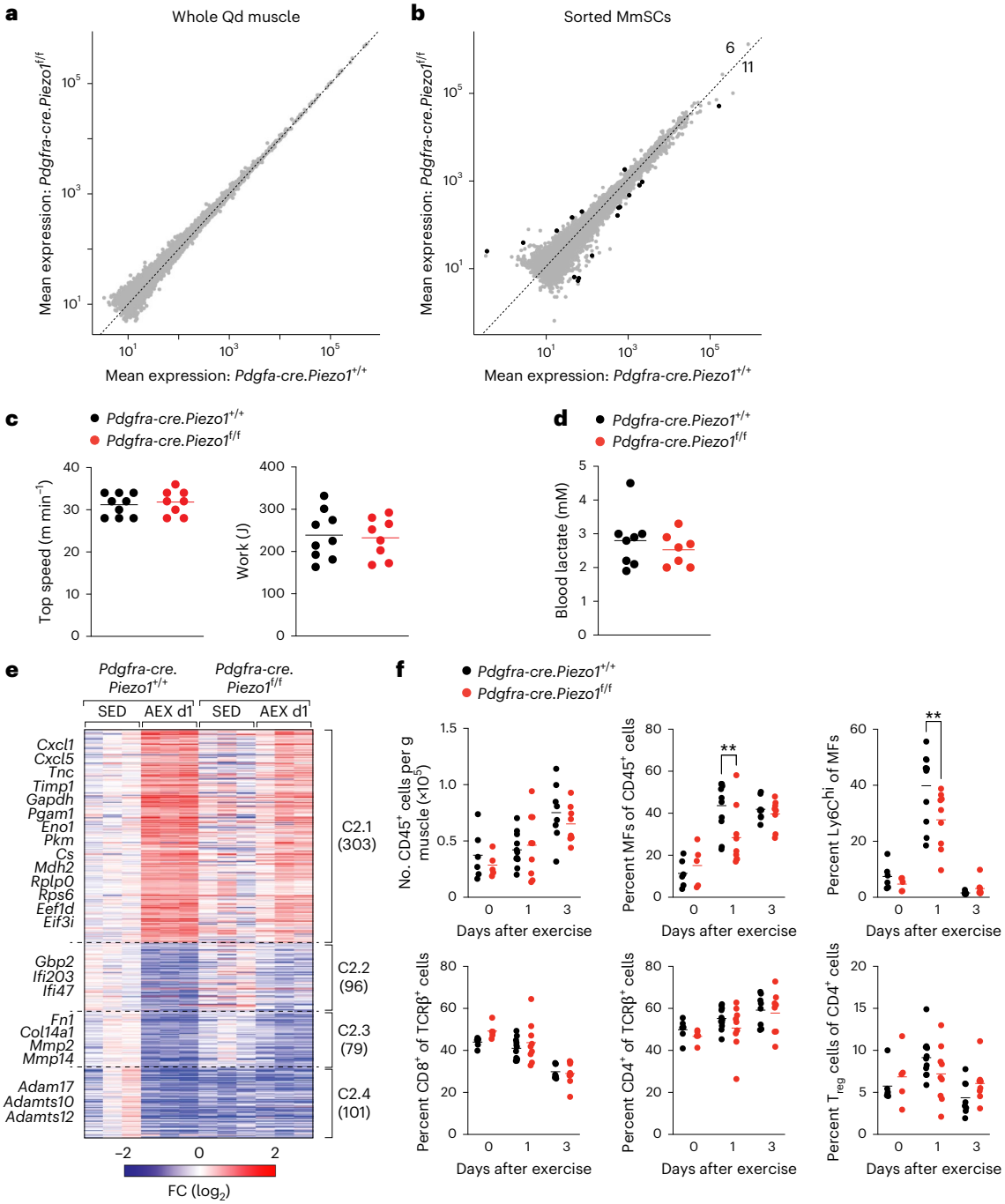

Fig. 4 | Exercise-induced MmSC activation and MF accrual depend on Piezo1. **a**,**b**, RNA-seq analysis of whole Qd muscles (**a**) or bulk MmSCs (**b**) from sedentary *Piezo1*-mutant versus wild-type mice ($n = 3$). Differentially expressed genes ($P_{adj} < 0.05$, $|FC| \geq 2$) are highlighted. **c**, Performance of sedentary mutant versus wild-type mice on an exercise capacity test ($n \geq 8$). **d**, Blood lactate concentrations measured immediately after AEX ($n \geq 7$). **e**, *k*-Means clustering of transcripts differentially expressed ($P_{adj} < 0.05$) in MmSCs from mutant or wild-type mice after versus before AEX ($n = 3$). Numbers in parentheses indicate the number of genes within each cluster. Fold change as compared to sedentary wild-type controls. **f**, Cytofluorometric analysis of hindlimb muscles from mutant versus wild-type mice before AEX and after 1 and 3 days of recovery ($n \geq 5$). Summary plots show data pooled from two or more independent experiments; $^{**}P < 0.01$ by a two-way ANOVA with Šídák's multiple comparisons test (**f**).

map to the same sites and have the potential to invoke inflammatory responses. To isolate mechanical stress from other niche factors, we sorted stromal cells from muscles of sedentary mice and cultured them in two- and three-dimensional (2D and 3D, respectively) systems with tunable mechanical properties (Fig. 3a–c). Culture of MmSCs on collagen-coated, 2D polyacrylamide (PA) gels made to mimic stiffness within a physiological range[36] resulted in an increased inflammatory reaction on the stiffest substrates, as indicated by increased IL-6 production (Fig. 3b). Similarly, MmSCs were also more activated when cultured in 3D collagen-based hydrogels of higher than lower density (Fig. 3c). Rheology on 3D hydrogels of similar construction has shown that gel stiffness increases with collagen density[37].

Mechanosensing is mediated by adhesion molecules, cytoskeletal components and ion channels[38]. We investigated the latter class of molecules for two reasons: (1) several previous studies on bone marrow stroma identified stretch-activated channels (SACs), in particular

Piezo1, as critical sensors of local mechanical stress[39–41], and (2) the other two modes of mechanosensing may at least partially operate through coordinate stimulation of SACs by causing membrane deformation. When incubated on standard tissue culture plates (Young's modulus of ~1×10^7 kPa), MmSCs treated with the known SAC inhibitor GsMTx-4 (refs. 42,43) showed lower IL-6 production (Fig. 3d). An inventory of the SACs expressed by MmSCs revealed *Piezo1* to be the most highly expressed, distantly followed by *Piezo2* (Fig. 3e).

Similar to mechanical stress modeled by culture on stiff substrates, simulated mechanical stress achieved by treatment of MmSCs with the specific Piezo1 agonist Yoda1 (ref. 44) led to a progressive increase in IL-6 production (Fig. 3f). Population-level RNA-seq revealed that Piezo1 agonism was sufficient to induce much of the broader inflammatory signature (Fig. 3g and Extended Data Fig. 3a). Moreover, *k*-means clustering of the inflammatory signature genes revealed three patterns of activation: early response (up at 2 h but down by 4 h), intermediate response (up at 4 and 6 h) and late response (up at 6 h). Most notable among the enriched transcripts were those encoding well-described immunomodulatory factors *Ccl2*, *Ccl7* and *Il33* (early) and *Il6*, *Tnc*, *Cxcl1*, *Lif* and *Ptgs2* (intermediate; Fig. 3g). There was also a strong effect of Piezo1 agonism on ECM-related factors: transcripts encoding collagens were downregulated (for example, *Col1a1*, *Col1a2*, *Col3a1*, *Col6a1* and *Col6a2*), whereas those encoding matrix metalloproteinases were enriched (for example, *Mmp10* and *Mmp12*; Extended Data Fig. 3b). This modulation of transcripts involved in ECM organization may indicate a compensatory reaction to reduce niche stiffness in response to mechanical stress.

Finally, we asked which signaling pathways might transduce Piezo1 agonism for stromal cell activation. Profiling the serine/threonine kinase activity of cardiac fibroblasts treated with Yoda1 highlighted mitogen-activated protein kinases (MAPKs) and cyclin-dependent kinases as the most highly enriched families[45]. Our transcriptional profiling of MmSCs treated with Yoda1 also showed enrichment in these pathways. To elucidate a mechanism by which Piezo1 ion gating promotes the inflammatory reaction in MmSCs, we focused on the MAPKs (ERK1/ERK2, p38 MAPK and JNK; Fig. 3h) due to their involvement in the regulation of inflammatory cytokine and chemokine expression at transcriptional (for example, activation of AP-1 family transcription factors) and post-transcriptional levels (for example, mRNA stabilization via a p38-MK2-dependent, AU-rich-region-targeted mechanism)[46,47]. We pretreated conventionally cultured MmSCs with inhibitors of ERK1/ERK2 (SCH772984, ravoxertinib), p38 MAPK (SB202190, adezmapimod) and JNK (JNK-IN-8, SP600125) before Piezo1 stimulation for 5 h. All three arms of the MAPK signaling pathway were necessary for increased IL-6 production by Yoda1 treatment (Fig. 3i). Although this result appears to be inconsistent with a prior report, in which induction of *Il6* transcripts in cardiac fibroblasts treated with Yoda1 for 24 h was dependent on p38 MAPK but not on ERK or JNK[45], mechanical stress in other contexts activates various combinations of the three MAPK signaling arms[48,49]. Thus, the mechanosensitive cation channel Piezo1 is a sensor capable of inducing an immunomodulatory program in MmSCs via MAPK signaling.

Piezo1 signaling promotes the exercise-induced MmSC inflammatory reaction

To address whether Piezo1-dependent activation of MmSCs was necessary for exercise-induced inflammation, we generated a mouse strain harboring conditional deletion of *Piezo1* specifically in mSCs (*Pdgfra-cre.Piezo1*$^{fl/fl}$ mice; Extended Data Fig. 4a,b). At steady state, the mutant mice were phenotypically similar to their wild-type littermates based on a broad multimodal assessment, including comparison of their whole-muscle and MmSC transcriptomes (Fig. 4a,b), whole-heart and liver transcriptomes (Extended Data Fig. 4c,d), maximal exercise capacity (Fig. 4c), liver glycogen and blood glucose (Extended Data Fig. 4e,f) and splenic immunophenotype (Extended Data Fig. 4g,h). As expected from their comparable baseline physiology, mutant and wild-type mice performed similarly during a bout of AEX (Fig. 4d). However, stromal cells in the muscles of mutant mice showed impaired induction of hundreds of genes, including those encoding key factors involved in translation (for example, *Rplp0*, *Rps6*, *Eef1d* and *Eif3i*) and intermediary metabolism (for example, *Gapdh*, *Pgam1*, *Eno1*, *Pkm*, *Cs* and *Mdh2*), as well as several inflammatory signature transcripts (for example, *Cx3cl1*, *Cxcl5*, *Tnc* and *Timp1*; Fig. 4e and Extended Data Fig. 5a,b). AEX-induced accrual of muscle MFs and Ly6C^{hi} MFs was significantly impaired in mice harboring stromal-cell-specific *Piezo1* deletion, and the fraction of T_{reg} cells trended lower in muscle on day 1 of recovery (Fig. 4f and Extended Data Fig. 5c). Thus, stromal mechanosensing via Piezo1 regulates exercise-induced muscle MF accrual.

Piezo1-dependent MmSC activation is necessary for appropriately timed inflammatory and myogenic processes following acute injury

We wondered whether Piezo1 ultimately regulated MmSC activation and muscle inflammation in the response to acute injury. Population-level transcriptional profiling of MmSCs from mutant versus wild-type littermates on day 1 following CTX-induced injury revealed impaired induction of many genes indicative of inflammatory cytokine signaling, including many interferon-stimulated genes (Fig. 5a,b). Time-resolved cytofluorometric analysis uncovered a broad disruption of the highly coordinated, multicellular response to muscle injury (Fig. 5c,d and Extended Data Fig. 6a,b). In general, there was less immunocyte accumulation in mutant muscles early and more late after injury (Fig. 5c,d). In particular, in mutant mice, there was a delayed increase in CD4$^+$ T cells, including RORγ$^+$ T_{reg} cells, which we recently highlighted as an early-responding, microbiota-dependent population that is required to rein in IL-17A-driven inflammation to promote muscle regeneration[50].

The magnitude and duration of inflammatory responses must be controlled to prevent delayed muscle repair and consequent functional impairments[51]. To assess the effect of conditional deletion of *Piezo1* in stromal cells on tissue-level responses to injury, we performed whole-muscle RNA-seq over a time course after CTX-induced injury. Principal component analysis revealed day 3 after injury as the time at which the largest variance between genotypes manifested (Fig. 5e). Gene Ontology analysis of transcriptomes at this time point highlighted

Fig. 5 | Stromal cell Piezo1 is necessary for appropriately timed inflammatory and myogenic processes following acute injury. a, RNA-seq analysis of MmSCs sorted from pooled hindlimb muscles from mice mutant versus wild-type mice 1 day after CTX-induced injury ($n = 3$). Differentially expressed genes ($P_{adj} < 0.05$, $|FC| \geq 2$) are highlighted; genes of high interest are annotated. **b**, fast gene set enrichment analysis (fGSEA) showing top Hallmark gene sets enriched or depleted in MmSCs from mutant versus wild-type mice 1 day after CTX-induced injury; IFNγ, interferon-γ; IFNα, interferon-α; NES, normalized enrichment score. **c**,**d**, Cytofluorometric analysis of hindlimb muscles from mutant (KO) versus wild-type (WT) mice on the indicated days after injury ($n \geq 4$). Frequencies (**c**) and numbers of cells per gram of muscle (**d**) are normalized to wild-type littermates within each experiment; T_{conv}, conventional T cell. **e**, Principal component (PC) analysis of whole-tissue transcriptomes from TA muscles of mutant and wild-type mice over a time course of recovery from CTX-induced injury ($n = 3$ or 4). **f**, Volcano plot of day 3 mutant versus wild-type transcriptomes overlaid with genes constituting the Hallmark myogenesis signature ($n = 4$). **g**, Exercise performance measured longitudinally during recovery after muscle injury. Curves are normalized to preinjury capacity of each mouse ($n \geq 8$). Percent change in work was calculated by taking the slope of the curve for each mouse within the indicated windows. Summary plots show data pooled from three independent experiments; $^*P < 0.05$ and $^{**}P < 0.01$by an unpaired two-tailed Student's *t*-test (**c**, **d** and **g**, right), two-way repeated measures ANOVA with Šídák's multiple comparisons test (**g**, left and bottom) or Fisher's exact test (**f**); NF, neutrophil; EO, eosinophil; MHCII, major histocompatibility complex class II; d.p.i., days postinjury; geno, genotype.

https://doi.org/10.1038/s41590-026-02435-4

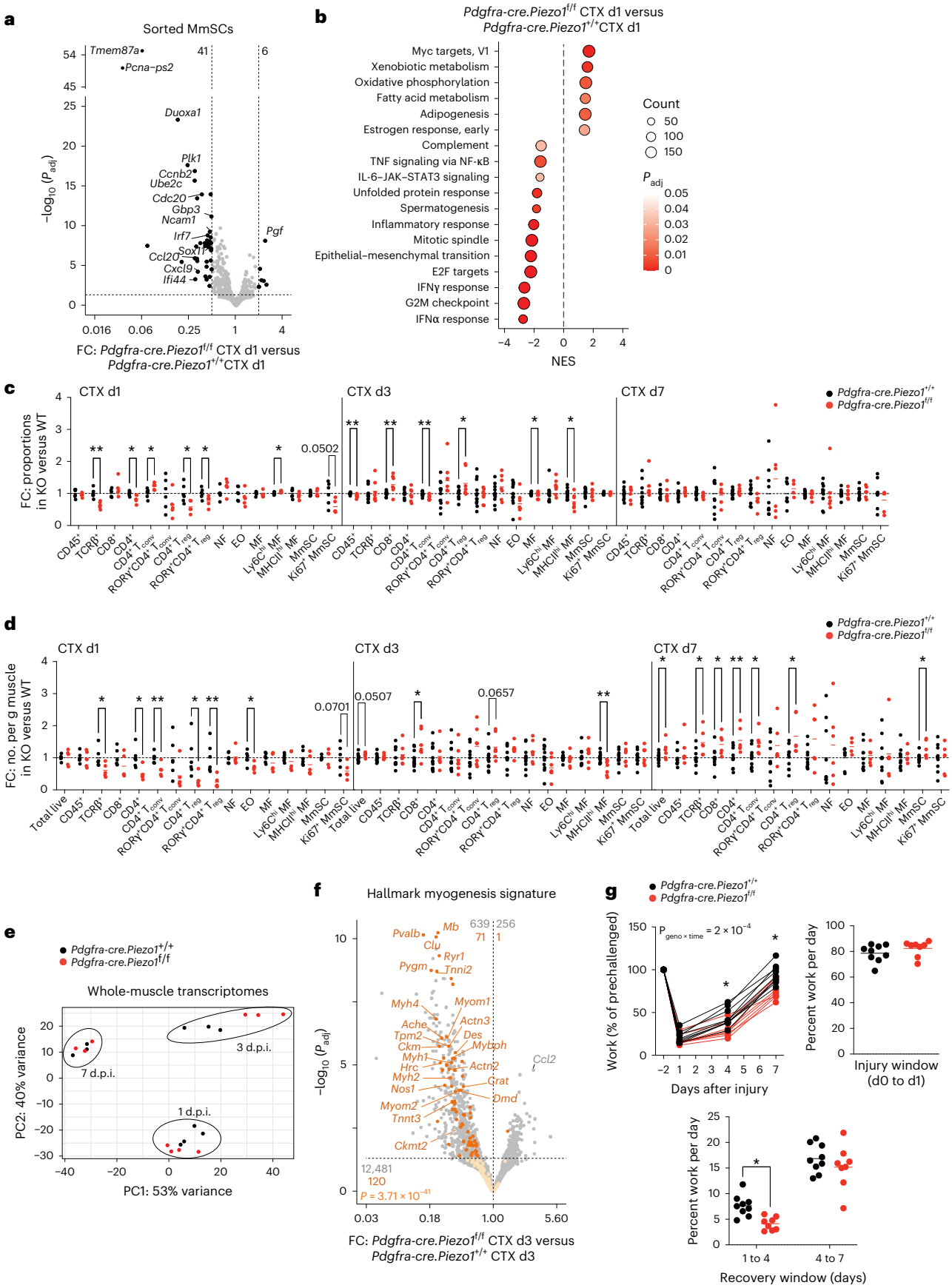

https://doi.org/10.1038/s41590-026-02435-4

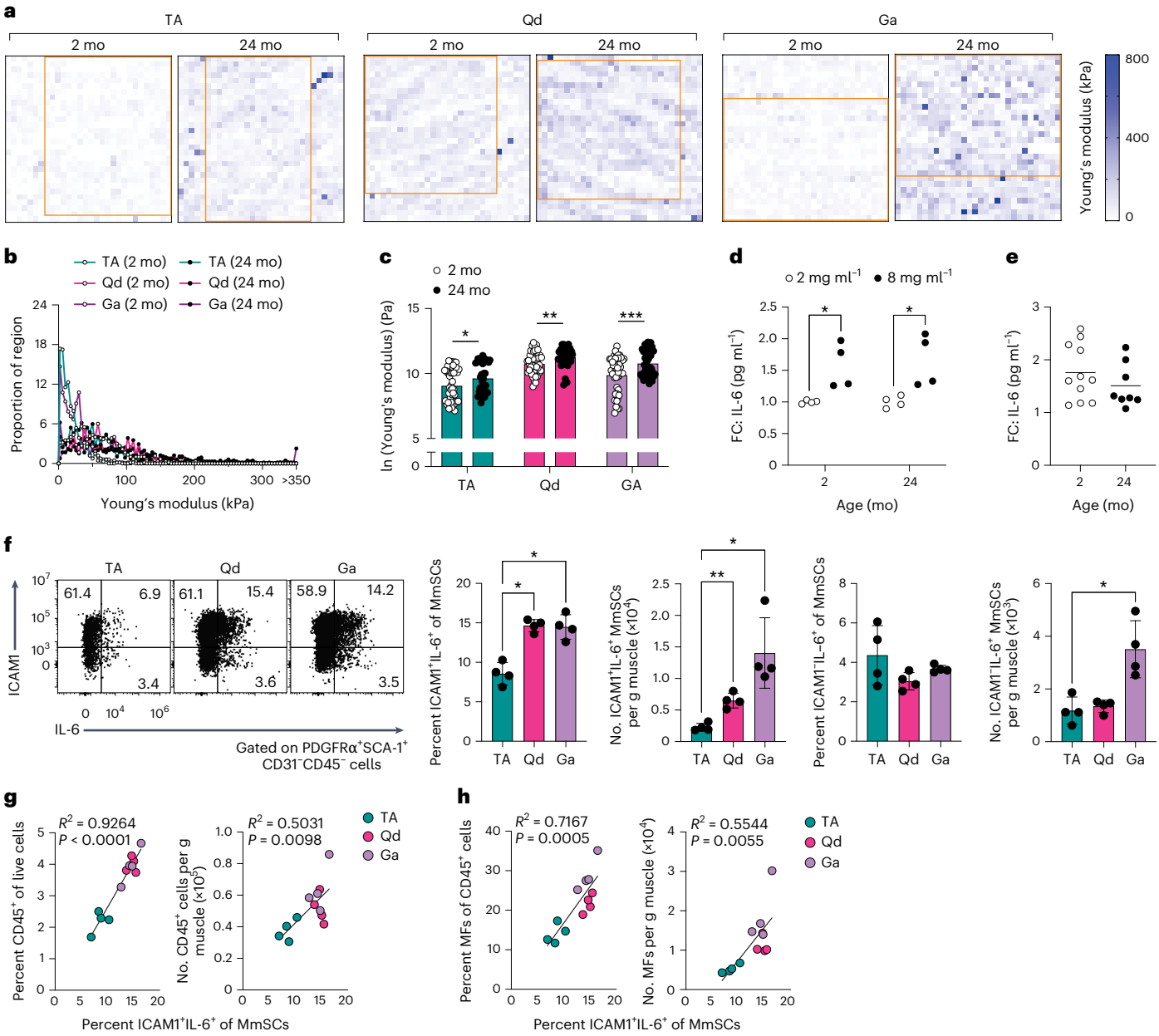

Fig. 6 | Natural aging is associated with site-specific muscle stiffening and parallel stromal activation and inflammation. a–**c**, Measurement of tissue stiffness (Young's modulus) by AFM on sections of TA, Qd and Ga muscles isolated from young (2 months (mo)) and aged (24 months) sedentary mice. Four mice were used per condition ($n = 4$), and a minimum of three regions were scanned from four sections per muscle (two superficial and two deep). **a**, Representative heat maps showing Young's moduli of TA, Qd and Ga muscles from sedentary young and aged mice. Each region is from a leveled area of 100 µm × 100 µm. Boxed subregions highlight areas selected to avoid topographical errors. **b**, Histograms of Young's modulus values from selected subregions in **a**. **c**, Summary of Young's moduli of TA, Qd and Ga muscles from young and aged mice. Data points are natural log transformed and represent average Young's modulus per region from three or more regions × four sections × four mice per group. Bar plots are drawn to show geometric means. **d**,**e**, IL-6 production by MmSCs isolated from young and aged mice and cultured in 3D collagen-based hydrogels of the indicated densities ($n = 4$; **d**) or treated with the Piezo1 agonist Yoda1 ($n \geq 8$; **e**). **f**, Representative flow cytometric plots of ICAM1 and TNC expression among MmSCs isolated from TA, Qd and Ga muscles of aged mice. Numbers inside the gates indicate frequencies of gated cells among total MmSCs. Summary frequencies and numbers per gram of muscle are shown to the right ($n = 4$). **g**,**h**, Correlation between the proportion of inflammatory MmSCs and total immunocytes (**g**) or MFs (**h**) across hindlimb muscles of aged mice ($n = 4$). Summary plots show data pooled from two or more independent experiments; $^{*}P < 0.05$, $^{**}P < 0.01$ and $^{***}P < 0.001$ by an unpaired two-tailed t-test with Welch's correction (**c**), a two-way ANOVA with Šídák's multiple comparisons test (**d**), a paired two-tailed Student's t-test (**e**), a one-way ANOVA with Dunnett's multiple comparisons test (**f**) or a simple linear regression (**g** and **h**).

lower expression of genes encoding sarcomere components in muscles from mutant versus wild-type mice (Extended Data Fig. 6c). In a targeted bioinformatic approach, overlay of a gene signature representing a consortium of molecules involved in myogenesis revealed significant de-enrichment in mutant muscles (Fig. 5f). Although the primary sites injured by CTX are known to be those directly injected (that is, hindlimb muscles), we also performed whole-heart RNA-seq to address the possibility of remote damage. Transcriptomic analysis revealed a small effect of intramuscular injection of CTX on the heart: only 27 genes were differentially expressed between day 3 after injury and uninjured controls ($P_{adj} < 0.05$, | FC | >2; Extended Data Fig. 6d). The remote effects of CTX on the heart were more pronounced in wild-type

mice than in *Piezo1*-mutant counterparts (Extended Data Fig. 6e), which was consistent with the impaired responses observed at the primary site of injury in mutant mice (Fig. 5a–f).

To determine whether the defective injury responses in *Piezo1*-mutant mice were physiologically meaningful, we measured the exercise capacity of mutant and wild-type littermates longitudinally, starting from 2 days before injury. Within 24 h of intramuscular injection of CTX, both genotypes showed an 80% reduction in exercise capacity (Fig. 5g). Wild-type mice had almost fully recovered by day 7, but *Piezo1*-mutant mice exhibited a slower recovery rate between days 1 and 4 after injury, resulting in impaired performance relative to their wild-type counterparts on days 4 and 7 (30.07% versus 44.25% and 75.61% versus 94.79% of pre-exercise capacity, respectively; Fig. 5g).

Age-associated stiffening of specific muscle groups promotes a parallel pattern of stromal cell activation and inflammatory reactivity

Aging is also associated with alterations in muscle mechanical properties, in particular increased stiffening of hindlimb muscles[52–54]. Such stiffening is associated with a higher muscle collagen content[52,53], which is partly driven by accumulation of $CD163^{+}CD206^{+}$ MFs[55,56]. These cells act as a source of ornithine (via high arginase activity) for subsequent conversion to proline and collagen synthesis. Age-associated muscle stiffening is also partially driven by decreased collagen fiber tortuosity and preferential loss of highly compliant ECM components, including elastin[54], and reduced collagen breakdown[57]. Interestingly, age-related reduction in the dynamic protein pool in skeletal muscle (that is, the pool of proteins that actively turn over) is much more pronounced in collagen protein from load-bearing muscle than in collagen protein from non-load-bearing muscle (for example, Ga versus TA)[57].

We wondered whether there might be differences in age-associated muscle stiffening at different anatomical sites. Indeed, atomic force microscopy (AFM) analysis of TA, Ga and Qd muscles from young (2 months) and aged (24 months) mice revealed preferential stiffening in the latter two muscle groups (Δ of 6.73, 31.76 and 28.01 kPa between TA, Qd and Ga muscles, respectively, from old and young mice; Fig. 6a–c). Somewhat surprisingly, MmSCs from aged mice were no less sensitive to activation by altering the mechanical properties of their niche or by Piezo1 agonism than were MmSCs from young mice (Fig. 6d,e). Cytofluorometric analysis revealed enrichment of inflammatory MmSCs in load-bearing muscles compared to TA muscle in aged mice (Fig. 6f); such enrichment was strongly correlated with greater immunocyte accrual, particularly of MFs (Fig. 6g,h). Thus, aging is associated with stromal cell activation and local inflammation specifically in muscle groups with larger age-related deviations in their mechanical properties.

Discussion

Exercise-induced inflammation must be controlled for the stereotypic metabolic adaptations and performance enhancement to ensue[5]; yet the root causes of such inflammation are not understood. Given their reported sensitivity to exercise[10,11,13,20,21] and capacity to recruit immunocytes to injured muscle[19], we addressed the role of MmSCs as sensors of exercise in skeletal muscle. Multipronged assessment of acute and chronic endurance exercise models highlighted an inflammatory reaction by MmSCs preferentially in load-bearing, immunologically active hindlimb muscles. Stromal cell immunomodulatory activities and consequent immunocyte recruitment at these sites were stimulated by Piezo1-dependent sensing of local mechanical stress, which was detected as group-preferential alterations in muscle stiffness immediately after exercise. Interestingly, mechanosensing by stromal cells was also necessary for appropriately timed inflammatory and myogenic responses to acute muscle injury and was associated with age-related muscle inflammation.

Although we focused on the role of Piezo1 expressed by stromal cells in sensing of mechanical stress in specific hindlimb muscles, exercise also stimulates mechanosensitive cells at other sites. Indeed, 4 weeks of voluntary wheel running reverses the age-related loss of common lymphoid progenitors in the marrow of load-bearing long bones but not in the calvarium; hindlimb unloading and deletion of *Piezo1* in osteolectin-expressing osteogenic progenitor cells produce the opposite phenotype[41]. The natural increase in blood pressure that occurs during physical activity is also regulated by mechanosensation, as this response is blunted during voluntary wheel running in mice harboring conditional deletion of *Piezo1* specifically in endothelial cells[58]. Most recently, the increase in gastrointestinal tract transit that occurs early during a bout of running was shown to depend on Piezo1 expressed by cholinergic enteric neurons[59]. Thus, it seems that Piezo1 is a bona fide exercise sensor, whose role in physiological responses to exercise depends on the identity of the cell type on which it is expressed and the time and location at which mechanical stress occurs.

The effect of conditional deletion of *Piezo1* on inflammation and recovery following muscle injury was more pronounced than that in the context of exercise; yet, in both cases, loss of functional Piezo1 in stromal cells blunted their inflammatory reaction and the consequent recruitment of immunocytes to perturbed muscles. Stimulation of Piezo1 on MmSCs, achieved via the specific agonist Yoda1, strongly induced expression of many genes encoding immunomodulatory factors, including *Ccl2*, *Ccn4*, *Cx3cl1*, *Cxcl1*, *Cxcl14*, *Cxcl5*, *Ptgs2* and *Tnc*. These findings are reminiscent of the previously reported role of Piezo1 in myeloid cells in other proinflammatory conditions. For example, myeloid cell-specific (*Lyz2-cre*) deletion of *Piezo1* impairs lung inflammation in response to infection with *Pseudomonas aeruginosa*; cyclical hydrostatic pressure, modeling what cells experience in the lungs, induces a complement of genes encoding proinflammatory mediators (for example, *Il6*, *Tnf*, *Il1b*, *Ccl7*, *Cxcl1* and *Ptgs2*) in bone marrow-derived MFs (BMDMs) in a Piezo1-dependent manner[60]. Piezo1 is also necessary for upregulation of proinflammatory gene expression in BMDMs treated with interferon-γ and lipopolysaccharide (treatment with Yoda1 or culture on stiff substrates augments proinflammatory polarization under these conditions)[61]. Piezo1 agonism is also sufficient to induce IL-6 and TNF production by bone marrow-derived dendritic cells[62]. Thus, based on our work and that of others, mechanosensation facilitated by Piezo1 seems to both initiate and amplify proinflammatory responses.

How does mechanosensation, in particular that enabled by Piezo1, prime an inflammatory response in this context? Piezo1 is a cation channel that rapidly opens following applied mechanical stress[63]. An initial increase in the concentration of intracellular calcium would prime signal transduction pathways to activate transcription of inflammatory cytokines and chemokines (for example, *Il6* and *Ccl2*), particularly downstream of ERK1/ERK2, p38 MAPK and JNK (Fig. 3i) and possibly NF-κB[61]. Such priming may influence reactivity to later signals, such as damage-associated molecular patterns or cytokines, that typically accompany mechanical stress and also rely on MAPK-dependent signaling[64]. Moreover, calcium positively regulates the activity of many key metabolic enzymes, including pyruvate dehydrogenase, isocitrate dehydrogenase, oxoglutarate dehydrogenase and mitochondrial glycerol-3-phosphate dehydrogenase[65], which may increase the provision of ATP for bioenergetically demanding processes that are augmented in activated stroma (for example, biosynthesis coupled to proliferation and translation coupled to cytokine production). Transcription-inducing histone modifications in the promoter regions of genes encoding inflammatory cytokines are also regulated by increased activity of these calcium-activated dehydrogenases. For example, in BMDMs stimulated with lipopolysaccharide, mitochondrial glycerol-3-phosphate dehydrogenase activity boosts glucose oxidation to bolster provision of acetyl coenzyme A for histone acetylation and induction of genes encoding inflammatory mediators, including IL-6 (ref. 66).

Why, in a teleological sense, does mechanosensation promote inflammatory responses? Based on the rapidity of the inflammatory reaction to mechanical stress, particularly the early induction of chemokine expression, Piezo1-dependent mechanosensation seems to serve as a mode of prospective recognition of inflammatory inducers[67], which would include damage-associated molecular patterns released as a consequence of subsequent loss of structure in load-bearing muscles[5]. Conversely, it is also possible that such site-specific loss of structure is partly responsible for the decreased stiffness of these sites after AEX. If Piezo1 recognizes loss of structure due to exercise-induced muscle damage, it would be serving as a mode of retrospective recognition[67]. This mode is likely operational in the later phase of recovery from an acute insult, such as when traumatic injury results in fibrosis. Indeed, chemically injured skeletal muscles show a large increase in their elastic moduli after the initial inflammatory response, and this change in tissue mechanical properties persists long after the initial insult[68]. Such stiffening could act as a tonic signal to mechanosensors that perpetuates an activated phenotype among MmSCs. This scenario is similar to the chronic state of stiffness-associated stromal cell activation and inflammation that we uncovered in aged, load-bearing muscles.

Regardless of whether it functions prospectively or retrospectively, if Piezo1-dependent mechanosensing is a proinflammatory module in skeletal muscle, then it stands as an attractive therapeutic target. We pursued this concept in the context of aging to reduce age-associated muscle inflammation; however, attempts to inhibit Piezo1 in specific hindlimb muscles were confounded by inflammation resulting from local drug delivery methods. As an alternative to pharmacological interventions to silence mechanosensing, elimination of the inducer (that is, mechanical stress) may also mitigate stiffness-associated inflammation. Interestingly, 10 weeks of treadmill running, 5 days per week, reduced the stiffness and total collagen content of muscles in aged rats[69]. Additional work is needed to determine whether preservation of tissue elasticity, and thus mitigation of local mechanical stress, is a mechanism underpinning the anti-inflammatory effect of long-term exercise, particularly in aged animals.

Although the present study relied on mouse models to elucidate the etiology of MmSC activation and consequent muscle inflammation in exercise, injury and aging, human muscle also harbors a substantial population of MmSCs[70], which contribute to the increased levels of many proinflammatory cytokines and chemokines found in aged versus young muscle[71]; acute exercise and injury elicit an inflammatory reaction among human MmSCs similar to that of mouse MmSCs[71,72]. Future studies are required to elucidate whether modulating the Piezo1–MmSC pair in humans dampens tissue inflammation.

Online content

Any methods, additional references, Nature Portfolio reporting summaries, source data, extended data, supplementary information, acknowledgements, peer review information; details of author contributions and competing interests; and statements of data and code availability are available at https://doi.org/10.1038/s41590-026-02435-4.

References

1. Furman, D. et al. Chronic inflammation in the etiology of disease across the life span. *Nat. Med.* **25**, 1822–1832 (2019).
2. Arem, H. et al. Leisure time physical activity and mortality: a detailed pooled analysis of the dose-response relationship. *JAMA Intern. Med.* **175**, 959–967 (2015).
3. Sanford, J. A. et al. Molecular Transducers of Physical Activity Consortium (MoTrPAC): mapping the dynamic responses to exercise. *Cell* **181**, 1464–1474 (2020).
4. MoTrPAC Study Group, Lead Analysts & MoTrPAC Study Group Temporal dynamics of the multi-omic response to endurance exercise training. *Nature* **629**, 174–183 (2024).
5. Langston, P. K. et al. Regulatory T cells shield muscle mitochondria from interferon-γ-mediated damage to promote the beneficial effects of exercise. *Sci. Immunol.* **8**, eadi5377 (2023).
6. Langston, P. K. & Mathis, D. Immunological regulation of skeletal muscle adaptation to exercise. *Cell Metab.* **36**, 1175–1183 (2024).
7. Becker, M. et al. Regulatory T cells require IL6 receptor α signaling to control skeletal muscle function and regeneration. *Cell Metab.* **35**, 1736–1751 (2023).
8. Van der Stede, T. et al. Cellular deconstruction of the human skeletal muscle microenvironment identifies an exercise-induced histaminergic crosstalk. *Cell Metab.* **37**, 842–856 (2025).
9. Pillon, N. J. et al. Distinctive exercise-induced inflammatory response and exerkine induction in skeletal muscle of people with type 2 diabetes. *Sci. Adv.* **8**, eabo3192 (2022).
10. Kang, X. et al. Exercise-induced musclin determines the fate of fibro-adipogenic progenitors to control muscle homeostasis. *Cell Stem Cell* **31**, 212–226 (2024).
11. Wei, W. et al. Organism-wide, cell-type-specific secretome mapping of exercise training in mice. *Cell Metab.* **35**, 1261–1279 (2023).
12. Knudsen, N. H. et al. Interleukin-13 drives metabolic conditioning of muscle to endurance exercise. *Science* **368**, eaat3987 (2020).
13. Yang, J. et al. Single-cell dissection of the obesity–exercise axis in adipose–muscle tissues implies a critical role for mesenchymal stem cells. *Cell Metab.* **34**, 1578–1593 (2022).
14. Liu, L. et al. Exercise reprograms the inflammatory landscape of multiple stem cell compartments during mammalian aging. *Cell Stem Cell* **30**, 689–705 (2023).
15. Joe, A. W. et al. Muscle injury activates resident fibro/adipogenic progenitors that facilitate myogenesis. *Nat. Cell Biol.* **12**, 153–163 (2010).
16. Uezumi, A. et al. Mesenchymal progenitors distinct from satellite cells contribute to ectopic fat cell formation in skeletal muscle. *Nat. Cell Biol.* **12**, 143–152 (2010).
17. Uezumi, A. et al. Fibrosis and adipogenesis originate from a common mesenchymal progenitor in skeletal muscle. *J. Cell Sci.* **124**, 3654–3664 (2011).
18. Wosczyna, M. N. et al. Mesenchymal stromal cells are required for regeneration and homeostatic maintenance of skeletal muscle. *Cell Rep.* **27**, 2029–2035 (2019).
19. Yaghi, O. K. et al. A discrete 'early-responder' stromal-cell subtype orchestrates immunocyte recruitment to injured tissue. *Nat. Immunol.* **24**, 2053–2067 (2023).
20. Valero, M. C. et al. Eccentric exercise facilitates mesenchymal stem cell appearance in skeletal muscle. *PLoS ONE* **7**, e29760 (2012).
21. Saito, Y. et al. Exercise enhances skeletal muscle regeneration by promoting senescence in fibro-adipogenic progenitors. *Nat. Commun.* **11**, 889 (2020).
22. Chiquet-Ehrismann, R. & Chiquet, M. Tenascins: regulation and putative functions during pathological stress. *J. Pathol.* **200**, 488–499 (2003).
23. Midwood, K. S., Hussenet, T., Langlois, B. & Orend, G. Advances in tenascin-C biology. *Cell. Mol. Life Sci.* **68**, 3175–3199 (2011).
24. Midwood, K. et al. Tenascin-C is an endogenous activator of Toll-like receptor 4 that is essential for maintaining inflammation in arthritic joint disease. *Nat. Med.* **15**, 774–780 (2009).
25. Zuliani-Alvarez, L. et al. Mapping tenascin-C interaction with toll-like receptor 4 reveals a new subset of endogenous inflammatory triggers. *Nat. Commun.* **8**, 1595 (2017).
26. Marzeda, A. M. & Midwood, K. S. Internal affairs: tenascin-C as a clinically relevant, endogenous driver of innate immunity. *J. Histochem. Cytochem.* **66**, 289–304 (2018).
27. Lukjanenko, L. et al. Aging disrupts muscle stem cell function by impairing matricellular WISP1 secretion from fibro-adipogenic progenitors. *Cell Stem Cell* **24**, 433–446 (2019).

28. Pillon, N. J. et al. Transcriptomic profiling of skeletal muscle adaptations to exercise and inactivity. *Nat. Commun.* **11**, 470 (2020).
29. Furrer, R. et al. Molecular control of endurance training adaptation in male mouse skeletal muscle. *Nat. Metab.* **5**, 2020–2035 (2023).
30. Timmons, J. A. et al. Using molecular classification to predict gains in maximal aerobic capacity following endurance exercise training in humans. *J. Appl. Physiol.* **108**, 1487–1496 (2010).
31. Vaynman, S., Ying, Z. & Gomez-Pinilla, F. Hippocampal BDNF mediates the efficacy of exercise on synaptic plasticity and cognition. *Eur. J. Neurosci.* **20**, 2580–2590 (2004).
32. Szuhany, K. L., Bugatti, M. & Otto, M. W. A meta-analytic review of the effects of exercise on brain-derived neurotrophic factor. *J. Psychiatr. Res.* **60**, 56–64 (2015).
33. Engler, A. J., Sen, S., Sweeney, H. L. & Discher, D. E. Matrix elasticity directs stem cell lineage specification. *Cell* **126**, 677–689 (2006).
34. Flück, M., Tunc-Civelek, V. & Chiquet, M. Rapid and reciprocal regulation of tenascin-C and tenascin-Y expression by loading of skeletal muscle. *J. Cell Sci.* **113**, 3583–3591 (2000).
35. Chiquet, M., Renedo, A. S., Huber, F. & Fluck, M. How do fibroblasts translate mechanical signals into changes in extracellular matrix production?. *Matrix Biol.* **22**, 73–80 (2003).
36. Tse, J.R. & Engler, A.J. Preparation of hydrogel substrates with tunable mechanical properties. *Curr. Protoc. Cell Biol.* Chapter 10, Unit 10.16 (2010).
37. Meizlish, M. L. et al. Mechanosensing regulates tissue repair program in macrophages. *Sci. Adv.* **10**, eadk6906 (2024).
38. Du, H. et al. Tuning immunity through tissue mechanotransduction. *Nat. Rev. Immunol.* **23**, 174–188 (2023).
39. Li, X. et al. Stimulation of Piezo1 by mechanical signals promotes bone anabolism. *eLife* **8**, e49631 (2019).
40. Zhou, T. et al. Piezo1/2 mediate mechanotransduction essential for bone formation through concerted activation of NFAT–YAP1–β-catenin. *eLife* **9**, e52779 (2020).
41. Shen, B. et al. A mechanosensitive peri-arteriolar niche for osteogenesis and lymphopoiesis. *Nature* **591**, 438–444 (2021).
42. Suchyna, T. M. et al. Identification of a peptide toxin from *Grammostola spatulata* spider venom that blocks cation-selective stretch-activated channels. *J. Gen. Physiol.* **115**, 583–598 (2000).
43. Bae, C., Sachs, F. & Gottlieb, P. A. The mechanosensitive ion channel Piezo1 is inhibited by the peptide GsMTx4. *Biochemistry* **50**, 6295–6300 (2011).
44. Syeda, R. et al. Chemical activation of the mechanotransduction channel Piezo1. *eLife* **4**, e07369 (2015).
45. Blythe, N. M. et al. Mechanically activated Piezo1 channels of cardiac fibroblasts stimulate p38 mitogen-activated protein kinase activity and interleukin-6 secretion. *J. Biol. Chem.* **294**, 17395–17408 (2019).
46. Whitmarsh, A. J. & Davis, R. J. Transcription factor AP-1 regulation by mitogen-activated protein kinase signal transduction pathways. *J. Mol. Med.* **74**, 589–607 (1996).
47. Winzen, R. et al. The p38 MAP kinase pathway signals for cytokine-induced mRNA stabilization via MAP kinase-activated protein kinase 2 and an AU-rich region-targeted mechanism. *EMBO J.* **18**, 4969–4980 (1999).
48. Chiquet, M. Regulation of extracellular matrix gene expression by mechanical stress. *Matrix Biol.* **18**, 417–426 (1999).
49. Kjaer, M. Role of extracellular matrix in adaptation of tendon and skeletal muscle to mechanical loading. *Physiol. Rev.* **84**, 649–698 (2004).
50. Hanna, B. S. et al. The gut microbiota promotes distal tissue regeneration via RORγ^{+} regulatory T cell emissaries. *Immunity* **56**, 829–846 (2023).
51. Tidball, J. G. Regulation of muscle growth and regeneration by the immune system. *Nat. Rev. Immunol.* **17**, 165–178 (2017).
52. Alnaqeeb, M. A., Al Zaid, N. S. & Goldspink, G. Connective tissue changes and physical properties of developing and ageing skeletal muscle. *J. Anat.* **139**, 677–689 (1984).
53. Wood, L. K. et al. Intrinsic stiffness of extracellular matrix increases with age in skeletal muscles of mice. *J Appl. Physiol.* **117**, 363–369 (2014).
54. Stearns-Reider, K. M. et al. Aging of the skeletal muscle extracellular matrix drives a stem cell fibrogenic conversion. *Aging Cell* **16**, 518–528 (2017).
55. Wang, Y., Wehling-Henricks, M., Samengo, G. & Tidball, J. G. Increases of M2a macrophages and fibrosis in aging muscle are influenced by bone marrow aging and negatively regulated by muscle-derived nitric oxide. *Aging Cell* **14**, 678–688 (2015).
56. Wang, Y. et al. Myeloid cell-specific mutation of *Spi1* selectively reduces M2-biased macrophage numbers in skeletal muscle, reduces age-related muscle fibrosis and prevents sarcopenia. *Aging Cell* **21**, e13690 (2022).
57. Abbott, C. B. et al. A novel stable isotope approach demonstrates surprising degree of age-related decline in skeletal muscle collagen proteostasis. *Function* **2**, zqab028 (2021).
58. Rode, B. et al. Piezo1 channels sense whole body physical activity to reset cardiovascular homeostasis and enhance performance. *Nat. Commun.* **8**, 350 (2017).
59. Xie, Z. et al. Enteric neuronal Piezo1 maintains mechanical and immunological homeostasis by sensing force. *Cell* **188**, 2417–2432 (2025).
60. Solis, A. G. et al. Mechanosensation of cyclical force by Piezo1 is essential for innate immunity. *Nature* **573**, 69–74 (2019).
61. Atcha, H. et al. Mechanically activated ion channel Piezo1 modulates macrophage polarization and stiffness sensing. *Nat. Commun.* **12**, 3256 (2021).
62. Chakraborty, M. et al. Mechanical stiffness controls dendritic cell metabolism and function. *Cell Rep.* **34**, 108609 (2021).
63. Coste, B. et al. Piezo1 and Piezo2 are essential components of distinct mechanically activated cation channels. *Science* **330**, 55–60 (2010).
64. Huang, G., Shi, L. Z. & Chi, H. Regulation of JNK and p38 MAPK in the immune system: signal integration, propagation and termination. *Cytokine* **48**, 161–169 (2009).
65. Denton, R. M. Regulation of mitochondrial dehydrogenases by calcium ions. *Biochim. Biophys. Acta* **1787**, 1309–1316 (2009).
66. Langston, P. K. et al. Glycerol phosphate shuttle enzyme GPD2 regulates macrophage inflammatory responses. *Nat. Immunol.* **20**, 1186–1195 (2019).
67. Medzhitov, R. The spectrum of inflammatory responses. *Science* **374**, 1070–1075 (2021).
68. Silver, J. S. et al. Injury-mediated stiffening persistently activates muscle stem cells through YAP and TAZ mechanotransduction. *Sci. Adv.* **7**, eabe4501 (2021).
69. Gosselin, L. E. et al. Effect of exercise training on passive stiffness in locomotor skeletal muscle: role of extracellular matrix. *J. Appl. Physiol.* **85**, 1011–1016 (1998).
70. Kuswanto, W. et al. Poor repair of skeletal muscle in aging mice reflects a defect in local, interleukin-33-dependent accumulation of regulatory T cells. *Immunity* **44**, 355–367 (2016).
71. Moiseeva, V. et al. Senescence atlas reveals an aged-like inflamed niche that blunts muscle regeneration. *Nature* **613**, 169–178 (2023).
72. Lovric, A. et al. Single-cell sequencing deconvolutes cellular responses to exercise in human skeletal muscle. *Commun. Biol.* **5**, 1121 (2022).

Methods

Mice

All mice were maintained under specific pathogen-free conditions at Harvard Medical School facilities in accordance with Institutional Animal Care and Use Committee guidelines (IS00001257 and IS00001725). C57BL/6J, C57BL/6-Tg(*Pdgfra-cre*)1Clc/J (*Pdgfra-cre*) and B6.Cg-*Piezo1*$^{tm2.1Apat}$/J (*Piezo1*$^{fl/fl}$)[73] mice were originally purchased from The Jackson Laboratory, and mice were bred and maintained in-house before use in experiments between 8 and 10 weeks of age. All experiments using these strains were conducted with littermate controls. Both male and female mice were used for cytofluorometric and performance assays. Aged mice were imported from the National Institute on Aging aged rodent colony, which is maintained at Charles River Laboratories by the Translational Research Branch within the National Institute on Aging Division of Aging Biology, at least 2 weeks before use for experiments.

Mouse treatments

Acute and chronic exercise models and exercise capacity testing were adapted from a previous study from our laboratory[5]. Briefly, for acute exercise and exercise capacity testing, mice were acclimatized to a motorized treadmill (Columbus Instruments, Exer 3/6 Treadmill) for 2 consecutive days, followed by a full bout at least 24 h later. Treadmill running began between Zeitgeber time (ZT) 0 and 1 and concluded before ZT4 to minimize circadian disruption. For acute exercise, a 5-min warm-up at 6 m min^{-1} was followed by a stepwise acceleration of 2 m min^{-1} every 2 min; the treadmill belt speed was capped at 18 m min^{-1} and sustained for 90 min. For exercise capacity testing, mice went through a similar warm-up, and the treadmill belt speed was then increased in increments of 2 m min^{-1}, every 5 min, until mice reached exhaustion, which was defined as the inability to remain on the treadmill belt for more than 5 s. Work was calculated as done previously[74]. For EXT, mice were housed individually in cages equipped with running wheels (Columbus Instruments, Home Cage Running Wheel). Voluntary wheel running was recorded at intervals of 10 s using software from the running wheels manufacturer.

For acute injury experiments, mice were anesthetized with ketamine:xylazine in combination (10 mg per kg (body weight): 2 mg per kg (body weight), intraperitoneal), followed by intramuscular injection with 30 µl of CTX from *Naja mossambica* (0.03 mg ml^{-1}; Sigma) into each hindlimb muscle (TA, Ga and Qd).

Cell isolation

Isolation of immunocytes from skeletal muscle was performed as previously described[75]. Briefly, hindlimb muscles were minced and incubated in digestion buffer (Ham's F10, 10% horse serum and collagenase II (800 U ml^{-1}); Gibco) for 90 min at 37 °C. Partially digested tissue and cells were sedimented by centrifugation, followed by further digestion using collagenase II (80 U ml^{-1}) and dispase (1 U ml^{-1}) for 30 min at 37 °C. Fully digested tissue was mechanically disrupted by passage through a syringe and filtered through a cell strainer. Isolated cells were washed and stained for cytofluorometric analysis or sorting. Isolation of immunocytes from spleens was performed as previously described[76]. Briefly, spleens were teased apart on a mesh screen, red blood cells were osmotically lysed using ACK Lysis Buffer (Gibco), and splenocytes were washed and stained for cytofluorometric analysis.

Cytofluorometric analysis and sorting

To identify the cell subsets examined in this study, we stained immunocytes with combinations of the following antibodies: anti-CD45 (30-F11), anti-CD31 (MEC13.3), anti-SCA1 (D7), anti-PDGFRα (APA5), anti-ICAM1 (YN1/1.7.4), anti-VCAM1 (429) anti-CD11b (M1/70), anti-CD64 (X54-5/7.1), anti-Ly6G (1A8), anti-Ly6C (HK1.4), anti-MHCII (M5/114.15.2), anti-SiglecF (S17007L), anti-TCRβ (H57-597), anti-CD4 (GK1.5), anti-CD8 (53-6.7) and anti-Helios (22F6; BioLegend); anti-TNC (4C8MS; Novus Biologicals); anti-Ki67 (B56; BD Pharmingen) and anti-ST2 (RMST2-2) and anti-RORγ (AFKJS-9; eBioscience). Viability was assessed using Zombie Fixable Viability kits (BioLegend). For identification of T_{reg} cells, cells were fixed, permeabilized and intracellularly stained for Foxp3 (FJK-16s) using the Foxp3/Transcription Factor Staining Buffer Set according to the manufacturer's instructions (eBioscience). For assessment of cytokine production, a protein transport inhibitor cocktail (eBioscience) was included in the first muscle digestion, and the second digestion step was omitted. Isolated cells were labeled by surface staining, followed by fixation/permeabilization using a Cytofix/Cytoperm kit (BD Biosciences). Intracellular CCL2 and IL-6 were detected by staining with anti-CCL2 (2H5) and anti-IL-6 (MP5-20F3; BioLegend). For assessment of MmSC proliferation, 1 mg of EdU was intraperitoneally injected into sedentary or acutely exercised (20 h after AEX) mice; muscles were collected for cell isolation 4 h later. EdU incorporation was measured using a Click-iT Plus EdU Alexa Fluor 488 Flow Cytometry Assay kit (Thermo Fisher Scientific) according to the manufacturer's instructions. Samples were acquired on a FACSymphony A5 flow cytometer (BD Biosciences) or Aurora spectral flow cytometer (Cytek); sorting was performed on a FACSAria (BD Biosciences). Data were analyzed using FlowJo software (Treestar).

Manipulation of cells ex vivo

For standard culture experiments, 10,000 cytofluorometrically sorted MmSCs were seeded into the bottom of 96-well plates in complete medium (RPMI 1640, 10% fetal bovine serum, 2 mM sodium pyruvate, 2 mM L-glutamine and 10 mM HEPES and penicillin/streptomycin). Piezo1 was activated by treatment with Yoda1 at a concentration of 25 µM (Sigma) for 2–24 h before collection of supernatants for enzyme-linked immunosorbent assay (ELISA) or lysis of cells for bulk RNA-seq. For inhibition of stretch-activated ion channels, MmSCs were treated with 10 µM GsMTx-4 (MedChemExpress). To inhibit MAPK signaling, MmSCs were treated with the following inhibitors for 1 h before 5 h of stimulation with Yoda1: 0.25 µM SCH772984, 1 µM ravoxertinib, 0.1 µM SB202190, 0.25 µM adezmapimod, 10 µM JNK-IN-8 and 5 µM SP600125 (MedChemExpress).

For culture on substrates with tunable mechanical properties, MmSCs were cytofluorometrically sorted and seeded onto or in 2D or 3D hydrogels. Cells were cultured for 24 h before supernatants were collected for ELISA. Two-dimensional hydrogels were constructed according to a previously published protocol[36]. Briefly, PA gels of elastic moduli ranging from 1 to 40 kPa were generated by polymerization of mixtures of acrylamide and bis-acrylamide in PBS at the following percentages: 5 and 0.03% (1 kPa), 5 and 0.225% (8 kPa) and 8 and 0.48% (40 kPa). PA gels were formed by sandwiching these mixtures between silanized glass (a coverslip coated with 3-aminopropyltriethoxysilane and a slide coated with dichlorodimethylsilane), and polymerization was achieved by the addition of ammonium persulfate and tetramethylethylenediamine (Sigma-Aldrich). Collagen I (PureCol, Advanced Biomatrix) was conjugated to PA gels using the heterobifunctional cross-linker Sulfo-SANPAH (sulfosuccinimidyl-6-[4′-azido-2′-nitrophenylamino]hexanoate; Thermo Fisher Scientific, A35395) in 50 mM HEPES. Sulfo-SANPAH was activated by placing PA gels under ultraviolet light. Collagen I binding was achieved by bathing PA gels in PureCol (250 µg ml^{-1}) overnight at 37 °C. Finally, 10,000 MmSCs were seeded onto the center of collagen-coated PA gels nested in non-tissue-culture-treated plates. MmSCs were allowed to attach to gels for up to 1 h before additional complete medium was added.

Three-dimensional gels were constructed following a modified version of a published protocol[37]. Briefly, sorted MmSCs (20,000 cells per condition) were resuspended in 50 µl of ice-cold high-concentration rat tail collagen I (Corning, 354249) neutralized and diluted to the desired final collagen concentrations by mixing with ice-cold sterile water, 10× PBS and 1 N NaOH (0.023 ml per ml of concentrated collagen I). Hydrogel–cell mixtures were added to non-tissue-culture-treated

96-well plates and incubated at 37 °C and 5% CO_2 until gelation was observed (up to 30 min). Complete medium was added to each well, and hydrogels were made to float by carefully disrupting their points of contact with the walls of the plate.

ELISA

Cell culture supernatants were spun down (5 min at 400*g*), diluted appropriately in 5% bovine serum albumin and assayed for IL-6 using a standard ELISA kit (BioLegend, 431304) according to the manufacturer's instructions. Samples were analyzed from at least two independent experiments. Relative IL-6 concentrations were calculated as the FC in IL-6 in each condition versus controls within an experiment.

RNA-seq and analysis

For population-level RNA-seq, samples were double sorted, and 1,000 MmSCs were collected into 5 µl of TCL buffer (Qiagen) containing 1% 2-mercaptoethanol (Sigma-Aldrich) in DNA LoBind tubes (Eppendorf). For whole-tissue RNA-seq, RNA was isolated from skeletal muscle (Qd or TA), heart (perfused) or liver (perfused) using TRIzol (Invitrogen) according to the manufacturer's instructions, and 2 ng of RNA was resuspended in 5 µl of TCL buffer containing 1% 2-mercaptoethanol in DNA LoBind tubes. Library construction, sequencing and data processing were performed as described before[5] according to the standard Immunological Genome Project protocols (https://www.immgen.org/img/Protocols/ImmGenULI_RNAseq_methods.pdf). Smart-seq2 libraries were prepared and sequenced as previously described[77]. Briefly, RNA was captured and purified using RNAClean XP beads (Beckman Coulter), and polyadenylated mRNA was selected using an anchored oligo(dT) primer (5′-AAGCAGTGGTATCAACGCAGAGTACT 30VN-3′). Polyadenylated mRNA was converted to cDNA by reverse transcription, followed by limited PCR amplification of first-strand cDNA. Tn5 transposon-based fragmentation was performed using a Nextera XT DNA Library Preparation kit (Illumina). To enable pooling before sequencing, samples were PCR amplified for an additional 12 cycles using barcoded primers such that each sample carried a specific combination of Illumina P5 and P7 barcodes. Paired-end sequencing was performed on an Illumina NextSeq500 (two full NextSeq runs per plate for an average of 10 million raw reads per sample) using two 38-base-pair reads with no further trimming. Reads were aligned to the mouse genome (GENCODE GRCm38/mm10 primary assembly and gene annotations vM16) using STAR 2.7.3a. Transcripts annotated as ribosomal RNA were removed, and gene-level quantification was calculated using the Subread 2.0 command featureCounts. The DESeq2 package from Bioconductor[78] was used to normalize raw read counts according to the median of ratios method (samples with fewer than 1 million uniquely mapped reads or with fewer than 8,000 genes with over 10 reads were excluded from normalization). Additional quality control after normalization included removal of biological replicates with a poor Pearson's correlation ($r < 0.9$). Genes with fewer than ten reads across samples within any condition were removed. Differential expression analysis was performed using DESeq2, and results were passed through the adaptive t prior shrinkage estimator from the apeglm package[79]. Differentially expressed genes were defined as adjusted *P* values of <0.05.

Heat maps, including modules identified by *k*-means clustering, were generated using Morpheus (Broad Institute). For pathway enrichment analysis, differentially expressed genes were analyzed by using the fgsea package[80] or Metascape[81]. Enriched pathways were defined as a false discovery rate of <0.05. For gene signature-based analyses, enrichment was defined as $P < 0.05$ according to Fisher's exact test.

Quantitative PCR with reverse transcription

RNA was extracted from 50,000–100,000 cytofluorometrically sorted immunocytes, endothelial cells, MmSCs and muscle stem cells using an RNeasy Mini kit (Qiagen) according to the manufacturer's instructions. cDNA synthesis was performed using a High-Capacity cDNA Reverse Transcription kit (Applied Biosystems). The expression of *Piezo1* was calculated by the change in cycle threshold ($2^{-\Delta\Delta C_t}$) method relative to the expression of *Hprt*. The following primer sequences were used: 5′-CTTGGGCTATATCCAGAACCAC-3′ (forward; *Piezo1*), 5′-CCAGCCCGAATTTGTAGAAGA-3′ (reverse; *Piezo1*), 5′-TTTCCCTGGTTAAGCAGTACAGCCC-3′ (forward; *Hprt*) and 5′-TGGCCTGTATCCAACACTTCGAGA-3′ (reverse; *Hprt*).

AFM

Mice were killed and immediately perfusion fixed using PBS followed by 4% paraformaldehyde. Hindlimb muscles were dissected, washed in PBS and equilibrated in Tissue-Tek OCT compound (Sakura) in intermediate-sized cryomolds (Fisher Scientific). Samples were rapidly frozen in liquid-N_2-cooled 2-methylbutane (Sigma-Aldrich) and cryosectioned at a thickness of 10 µm (longitudinal) in steps of 200 µm. A minimum of four sections, two superficial and two deep, from each sample were used for downstream analysis. Four mice were used per condition. Sections were stored temporarily in a humidifier at 4 °C and analyzed within 8–10 h.

AFM was performed on room-temperature sections using a Bruker JPK Nanowizard 4XP atomic force microscope and associated BioAFM SPM software. Probes (Bruker silicon nitride cantilever equipped with a 5-µm polystyrene bead tip; SAA-SPH-5UM) were mounted and calibrated before every session using 'contact' mode with PBS as the medium. Samples were indented with a set point of ~1 nN across a leveled area of 100 µm × 100 µm to minimize topographical errors. Measurements were acquired in Quantitative Imaging contact mode using PBS as the medium. Chosen regions were scanned using the raster scan method with a resolution of 30 × 30 pixels (900 measurements), a scan speed of 30 µm s^{-1} and a *z* length of 2,500 nm (for an indentation depth of up to 1 µm)[82–84]. A minimum of three different regions were scanned per slide.

Analysis of the resultant force-displacement (F-D) curves was performed using the Hertz model[82–85] for Young's modulus determination in Bruker BioAFM Data Processing software. Briefly, a representative F-D curve was chosen for each scanned region, and baseline subtraction was performed to correct for noise during acquisition. The contact point with the tissue was determined, and the displacement of the cantilever tip was calculated to generate a corrected F-D curve. Corrected F-D curve data were fitted to the Hertz model using a Poisson's ratio appropriate for soft tissues (0.5)[84,85]. The resultant fit was applied to all F-D curves from the same region via batch processing. Young's modulus heat maps were then generated for each region using Bruker BioAFM Data Processing software. The average Young's modulus of each region was determined by choosing a uniform rectangular area of interest whose height profile was well within the known thickness of each tissue section (boxed regions in figures). Because the per-region Young's moduli for each condition fit to a log-normal distribution, the data were natural log transformed for final visualization of summary values. Outlier analysis was performed for each condition across all mice using the ROUT test (GraphPad Prism) with a *Q* value threshold of 0.05.

Blood measurements

Glucose levels, in blood samples collected from the tail, were measured after a 4-h fast using a Contour glucose meter. Blood lactate levels were measured immediately after AEX using a Nova Biomedical Lactate Plus Meter.

Liver glycogen quantification

Glycogen was extracted from the left lobe of livers from *Piezo1*-mutant and wild-type mice and quantified as described previously[5,86]. Briefly, mice were perfused, and fresh liver tissue was snap-frozen in liquid N_2 immediately after dissection. Fresh-frozen livers were pulverized on dry ice using a precooled mortar and pestle, and powdered tissue was

weighed before subsequent metabolite extraction using 1 M HCl at 95 °C for 2 h. Extracts were neutralized using 2 M NaOH and clarified by centrifugation before dilution and quantification of glucose using a hexokinase assay kit according to the manufacturer's instructions (Sigma-Aldrich, GAHK20). Absorbance was measured at 340 nm, and glucose generated from hydrolysis of glycogen was quantified based on a standard curve and normalized to starting tissue weights.

Statistical analyses

Data are presented as mean ± s.d. Unless stated otherwise, GraphPad Prism software was used to perform statistical testing (Student's *t*-test for two-group comparisons or one-way ANOVA or two-way ANOVA for multiple-group comparisons). *P* values for gene signature enrichment in data presented in volcano plots were determined using Fisher's exact test; $^{*}P < 0.05$, $^{**}P < 0.01$, $^{***}P < 0.001$ and $^{****}P < 0.0001$. Mice with the same genotypes were randomly assigned to interventions in all cases. Exercise capacity tests were performed blinded.

Reporting summary

Further information on research design is available in the Nature Portfolio Reporting Summary linked to this article.

Data availability

Transcriptomes from RNA-seq analysis of whole skeletal muscles, hearts, liver specimens and sorted MmSCs have been deposited in the Gene Expression Omnibus (GSE297515). Source data are provided with this paper.

References

73. Cahalan, S. M. et al. Piezo1 links mechanical forces to red blood cell volume. *eLife* **4**, e07370 (2015).
74. Handschin, C. et al. Skeletal muscle fiber-type switching, exercise intolerance, and myopathy in PGC-1α muscle-specific knock-out animals. *J. Biol. Chem.* **282**, 30014–30021 (2007).
75. Liu, L., Cheung, T. H., Charville, G. W. & Rando, T. A. Isolation of skeletal muscle stem cells by fluorescence-activated cell sorting. *Nat. Protoc.* **10**, 1612–1624 (2015).
76. Langston, P. K. et al. Au-ACRAMTU-PEt3 alters redox balance to inhibit T cell proliferation and function. *J. Immunol.* **195**, 1984–1994 (2015).
77. Picelli, S. et al. Full-length RNA-seq from single cells using Smart-seq2. *Nat. Protoc.* **9**, 171–181 (2014).
78. Love, M. I., Huber, W. & Anders, S. Moderated estimation of fold change and dispersion for RNA-seq data with DESeq2. *Genome Biol.* **15**, 550 (2014).
79. Zhu, A., Ibrahim, J. G. & Love, M. I. Heavy-tailed prior distributions for sequence count data: removing the noise and preserving large differences. *Bioinformatics* **35**, 2084–2092 (2019).
80. Korotkevich, G. et al. Fast gene set enrichment analysis. Preprint at *bioRxiv* https://doi.org/10.1101/060012 (2021).
81. Zhou, Y. et al. Metascape provides a biologist-oriented resource for the analysis of systems-level datasets. *Nat. Commun.* **10**, 1523 (2019).
82. Calò, A. et al. Spatial mapping of the collagen distribution in human and mouse tissues by force volume atomic force microscopy. *Sci. Rep.* **10**, 15664 (2020).
83. Acerbi, I. et al. Human breast cancer invasion and aggression correlates with ECM stiffening and immune cell infiltration. *Integr. Biol.* **7**, 1120–1134 (2015).
84. Peloquin, J., Huynh, J., Williams, R. M. & Reinhart-King, C. A. Indentation measurements of the subendothelial matrix in bovine carotid arteries. *J. Biomech.* **44**, 815–821 (2011).
85. Shen, Y., Schmidt, T. & Diz-Munoz, A. Protocol on tissue preparation and measurement of tumor stiffness in primary and metastatic colorectal cancer samples with an atomic force microscope. *STAR Protoc.* **1**, 100167 (2020).
86. Sato, S. et al. Time of exercise specifies the impact on muscle metabolic pathways and systemic energy homeostasis. *Cell Metab.* **30**, 92–110 (2019).

Acknowledgements

We thank O. Yaghi, K. Hattori and A. Ortiz-Lopez for experimental assistance; L. Yang for bioinformatics support; C. Laplace for assistance with graphics; N. Colella for assistance with AFM and the Harvard Medical School Immunology Department Flow Cytometry Core. This work was performed in part at the Harvard University Center for Nanoscale Systems, a member of the National Nanotechnology Coordinated Infrastructure Network, which is supported by the National Science Foundation under NSF award number ECCS-2025158. Figure panels created with BioRender: the anatomical map of mouse hindlimb muscles in Fig. 2, the models in Fig. 3 and the scheme for AFM experiments in Extended Data Fig. 2. This work was funded by National Institutes of Health grant R01 AR070334 (D.M.), National Institutes of Health grant F32 AG072874 (P.K.L.) and The Freedom Together Foundation (D.M.).

Author contributions

Conceptualization: P.K.L. and D.M. Investigation: P.K.L. and J.V.R. Funding acquisition: D.M. Supervision: C.B. and D.M. Writing, original draft: P.K.L. and D.M. Writing, review and editing: all authors.

Competing interests

The authors declare that they have no competing interests.

Additional information

Extended data is available for this paper at https://doi.org/10.1038/s41590-026-02435-4.

Supplementary information The online version contains supplementary material available at https://doi.org/10.1038/s41590-026-02435-4.

Correspondence and requests for materials should be addressed to Diane Mathis.

Peer review information *Nature Immunology* thanks the anonymous reviewers for their contribution to the peer review of this work. Primary Handling Editor: S. Houston in collaboration with the *Nature Immunology* team.

https://doi.org/10.1038/s41590-026-02435-4

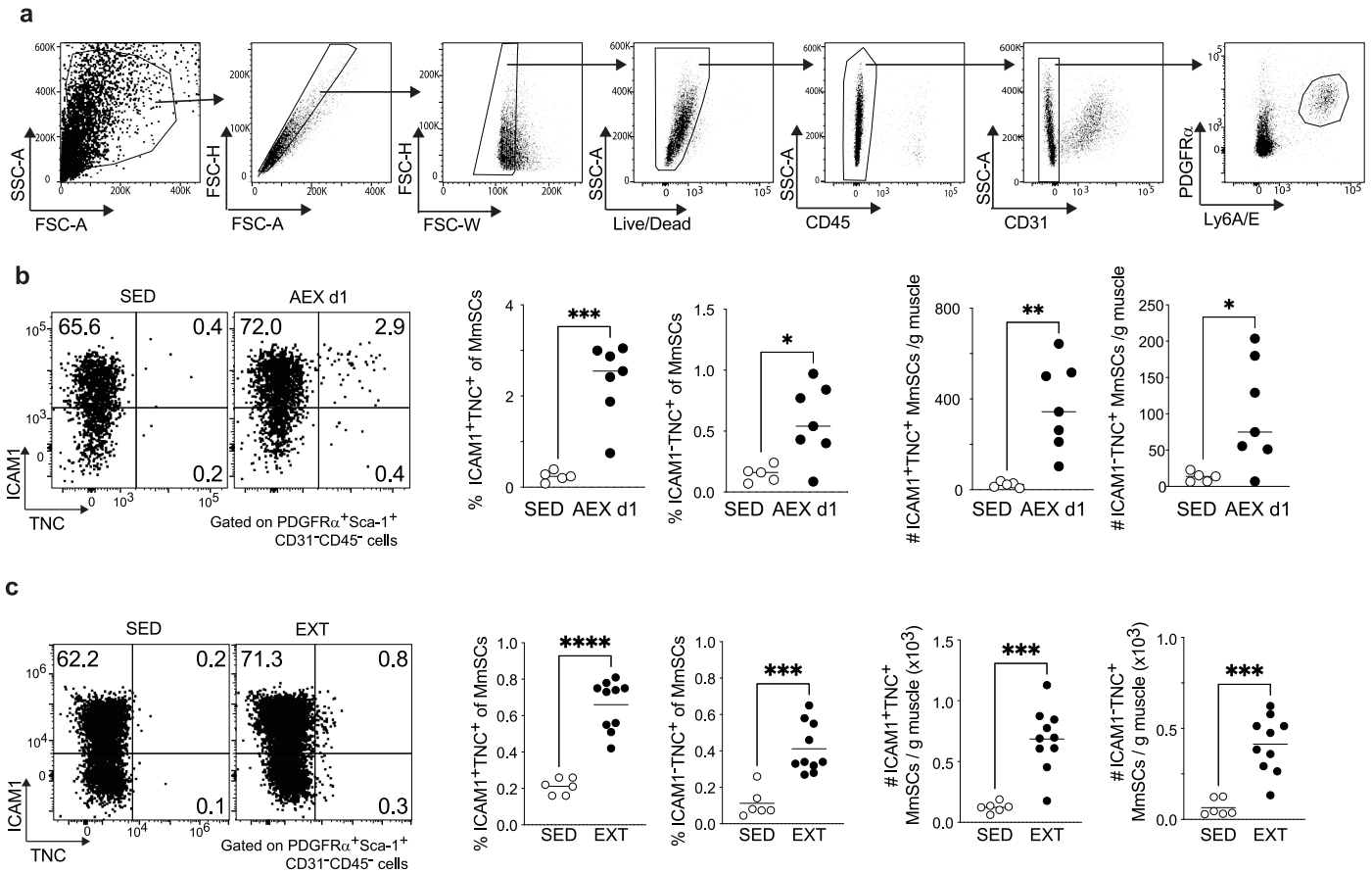

Extended Data Fig. 1 | Exercise-induced activation of stromal cells is reminiscent of that induced by injury. (**a**) Representative gating strategy used in the cytofluorometric analyses of MmSCs. (**b, c**) Representative flow-cytometric plots of TNC+ and ICAM1+ MmSCs before and 24 h after AEX (**b**) or 24 h after 2 weeks of EXT (**c**). Numbers inside gates indicate frequencies of gated cells among total MmSCs. Summary frequencies and numbers per gram of muscle are shown to the right (n ≥ 5). Summary plots show data pooled from ≥2 independent experiments. *$p < 0.05$, **$p < 0.01$, ***$p < 0.001$, ****$p < 0.0001$ by an unpaired two-tailed Student's t-test (**b,c**). SED, sedentary; AEX, acute exercise; EXT, exercise training; MmSC, muscle mesenchymal stromal cell; TNC, Tenascin-C.

https://doi.org/10.1038/s41590-026-02435-4

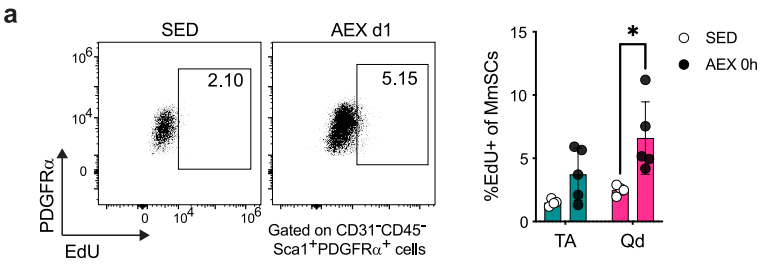

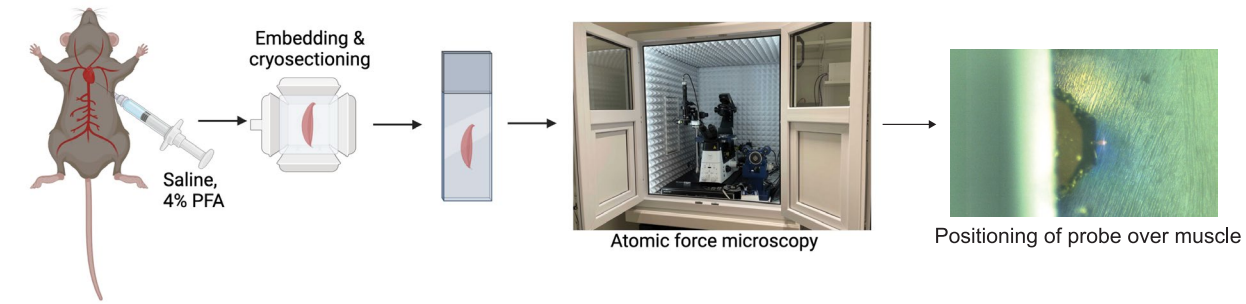

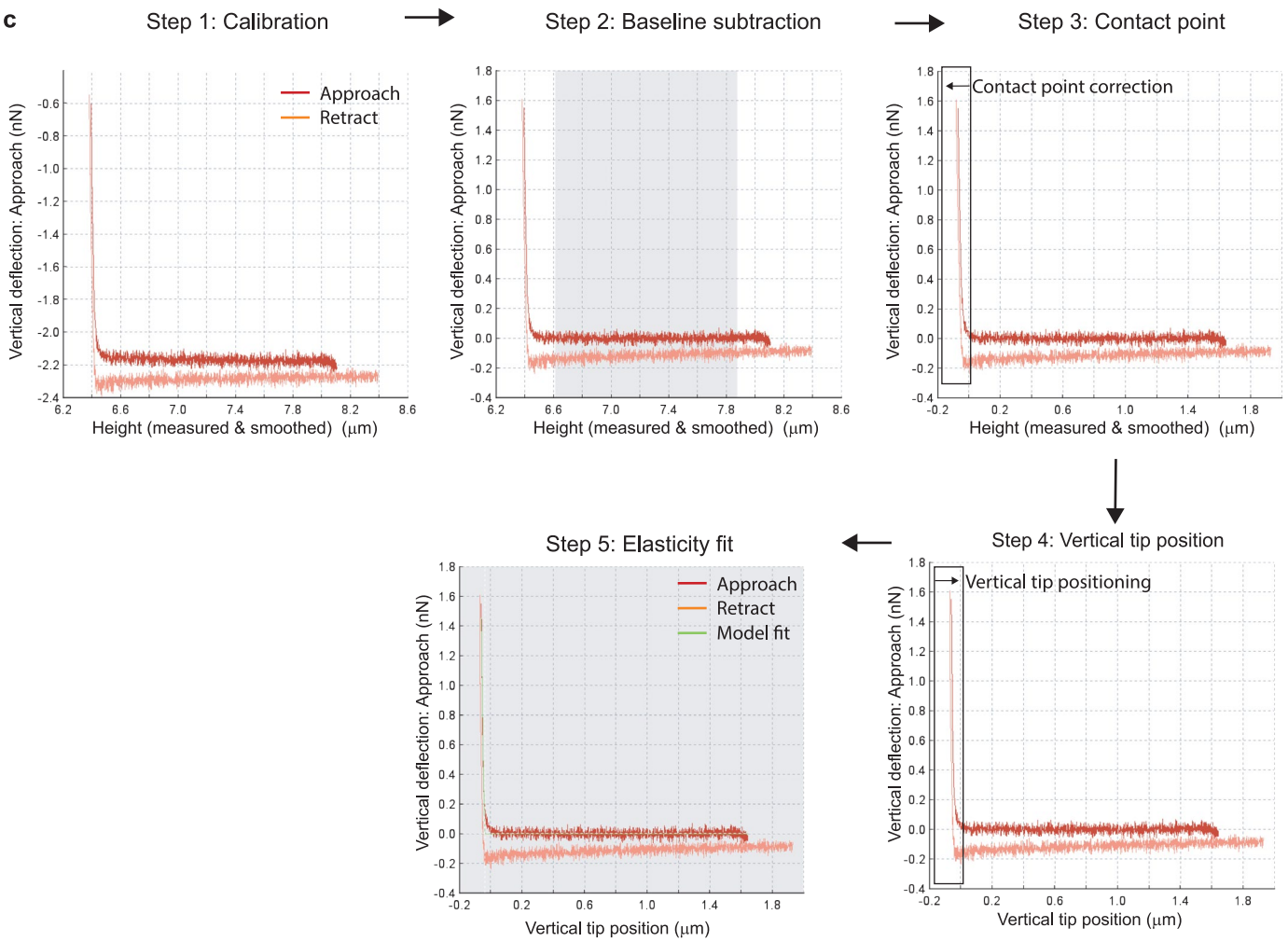

Extended Data Fig. 2 | See next page for caption.

https://doi.org/10.1038/s41590-026-02435-4

Extended Data Fig. 2 | Measurement of muscle stiffness by atomic force microscopy. (**a**) Representative flow-cytometric plots of EdU+ MmSCs before and 24 h after AEX (4 h EdU pulse, i.p.). Numbers inside gates indicate frequencies of gated cells among total MmSCs. Summary frequencies are shown to the right ($n \geq 4$) and represent 2 independent experiments. (**b**) Scheme for atomic force microscopy (AFM) on skeletal muscle sections. (**c**) Representative force-displacement (F-D) curves showing workflow for the analysis of AFM data to calculate Young's moduli of skeletal muscle sections. A full description of sample preparation and downstream analysis is included in the Materials and Methods. $^{*}p < 0.05$ by a two-way ANOVA with Šídák's multiple comparisons test (**a**). Panel created in BioRender: **b**, Langston, K. https://biorender.com/7y3v6d7 (2026).

https://doi.org/10.1038/s41590-026-02435-4

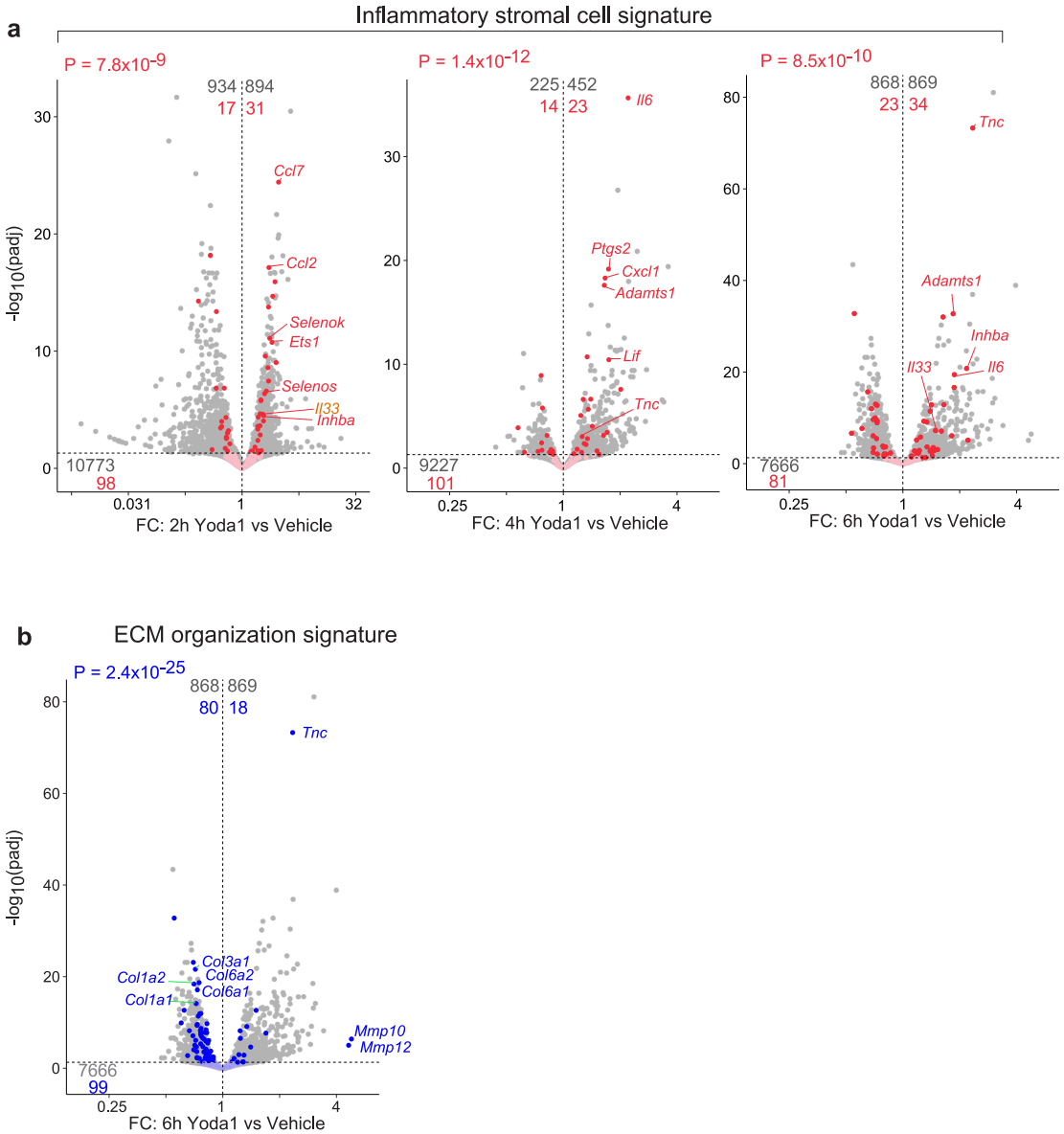

Extended Data Fig. 3 | Chemically induced mechanical stress modulates the expression of genes encoding immunomodulatory and ECM-associated factors in MmSCs. (**a**, **b**) RNA-seq analysis of MmSCs cultured on standard tissue-culture plates and treated with the Piezo1-specific agonist, Yoda1, or vehicle for the indicated times (n ≥ 2). Volcano plots are overlain with genes differentially enriched in the early-responder, inflammatory subtype of mesenchymal stromal cells found in acutely injured muscle[19] (**a**) or overlain with genes constituting the ECM organization signature from the GO database (**b**). *p* values computed by Fisher's exact test (**a, b**).

https://doi.org/10.1038/s41590-026-02435-4

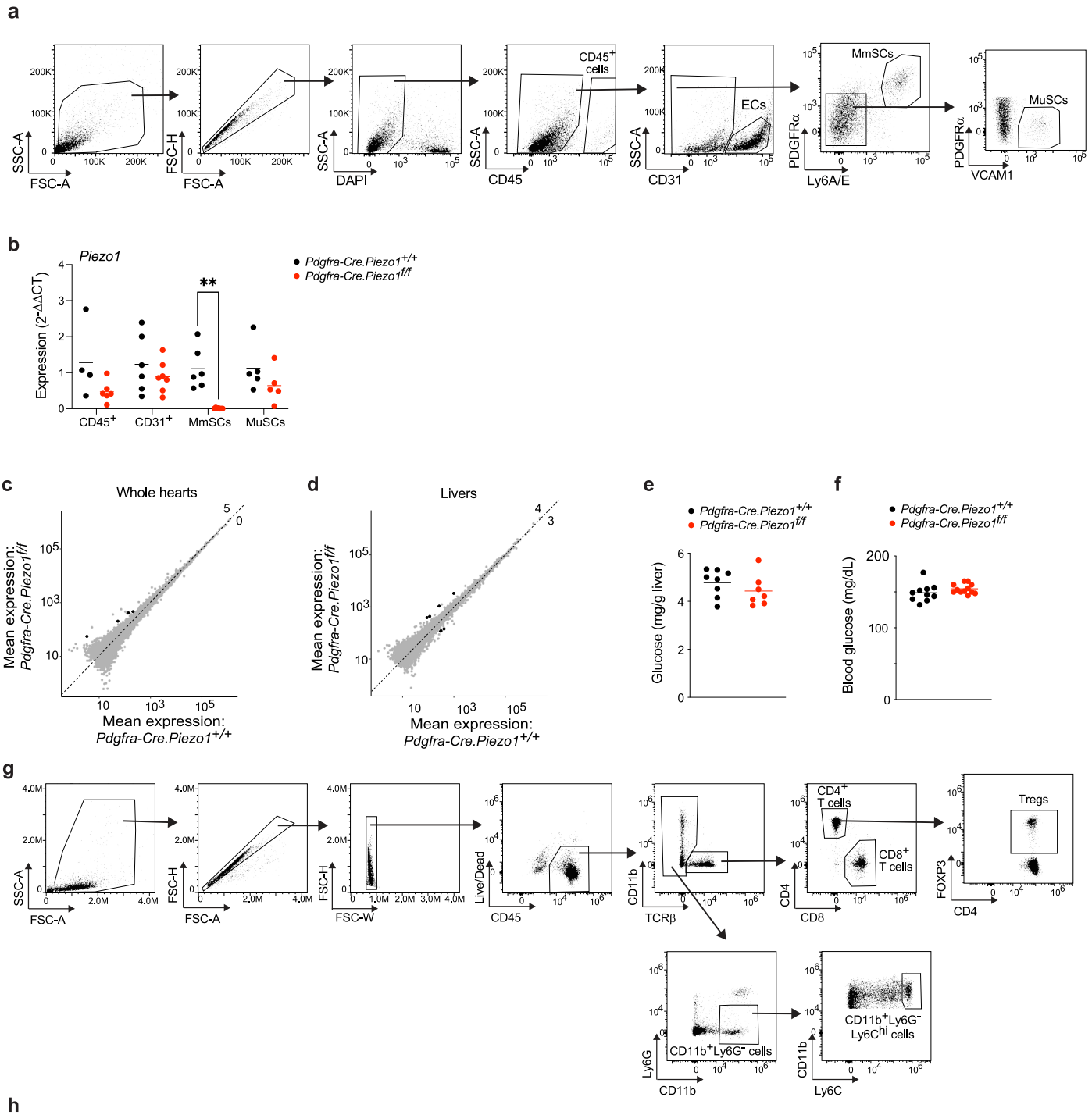

Extended Data Fig. 4 | See next page for caption.

https://doi.org/10.1038/s41590-026-02435-4

Extended Data Fig. 4 | Mice with stromal-cell-specific Piezo1 deficiency are largely phenotypically normal at steady state. (**a**) Representative gating strategy used in the cytofluorometric sorting of immunocytes (CD45+ cells), ECs, MmSCs, and MuSCs. (**b**) Expression of *Piezo1* in the indicated cell types sorted from muscles of *Piezo1* mutant versus wild-type mice (n≥4). Values are relative to expression of *Hprt*. (**c**, **d**) RNA-seq analysis of whole hearts (n = 3) (**c**) or livers (n = 4) (**d**) from sedentary *Piezo1* mutant versus WT mice. Differentially expressed genes (Padj < 0.05, |FC| ≥ 2) are highlighted. (**e**) Glycogen content of livers from *Piezo1* mutant and wild-type mice (n ≥ 7). (**f**) Fasting blood glucose levels of *Piezo1* mutant and wild-type mice (n ≥ 10). (**g**) Representative gating strategy used in the cytofluorometric analysis of spleens from *Piezo1* mutant and wild-type mice. (**h**) Numbers of non-neutrophil myeloid-lineage cells, monocytes, CD8 + T cells, CD4 + T cells, and Tregs in spleens of *Piezo1* mutant and wild-type mice, normalized to wet tissue weights (n = 10). Summary plots show data pooled from ≥2 independent experiments. $^{**}p < 0.01$ by two-way ANOVA with Šídák's multiple comparisons test (**b**). ECs, endothelial cells; MuSCs, muscle stem cells. All other abbreviations as per prior figures.

https://doi.org/10.1038/s41590-026-02435-4

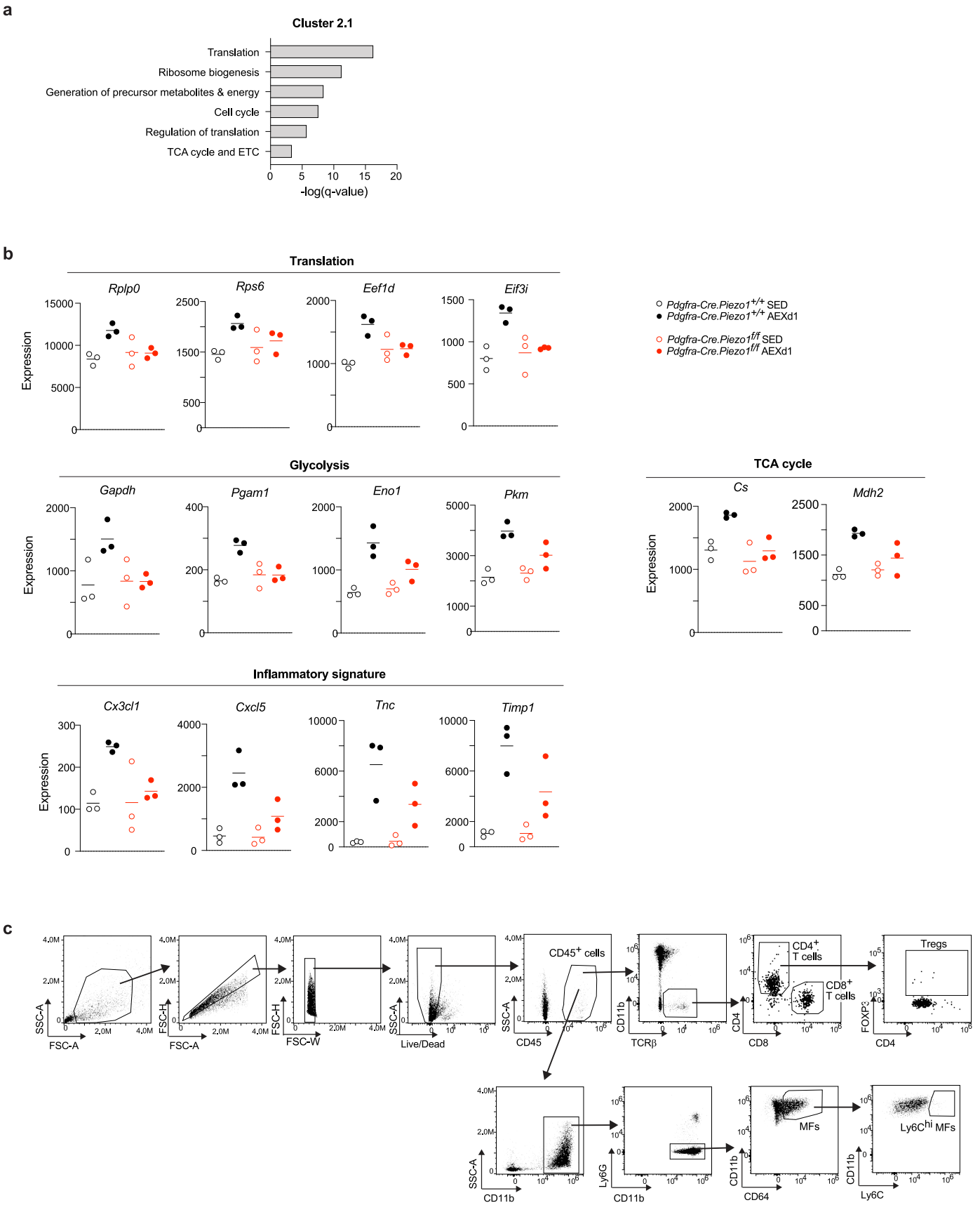

Extended Data Fig. 5 | Stromal-cell Piezo1 is necessary for their activation in response to exercise. (**a**) Metascape analysis showing top pathways enriched in Cluster 2.1 (Fig. 4). (**b**) Expression values for key genes in Cluster 2.1 (n = 3). (**c**) Representative gating strategy used in the cytofluorometric analysis of muscles from *Piezo1* mutant and wild-type mice before and after AEX.

https://doi.org/10.1038/s41590-026-02435-4

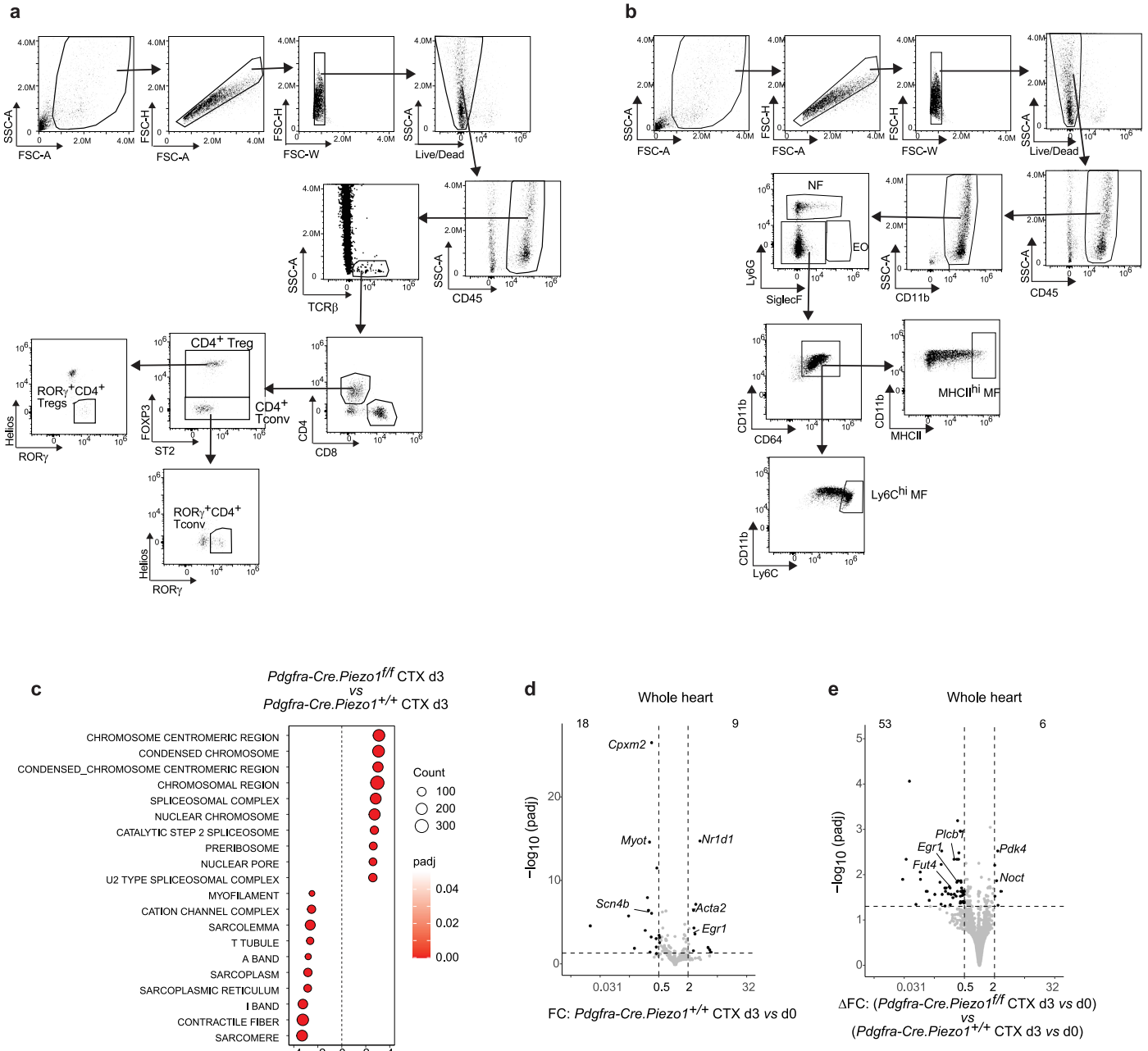

Extended Data Fig. 6 | Stromal-cell Piezo1 is necessary for appropriately timed myogenic processes following acute injury. (**a**, **b**) Representative gating strategies used in the cytofluorometric analysis of lymphoid- (**a**) and myeloid-lineage cells (**b**) from muscles of *Piezo1* mutant and wild-type mice after CTX-induced injury. (**c**) fGSEA showing top GO:CC gene sets enriched or depleted in TA muscles of mutant versus WT mice three days after CTX-induced injury. (**d**, **e**) RNA-seq analysis of whole hearts (perfused) from mice before or 3 d after CTX-induced injury to hindlimb muscles (n = 3). Highlighted genes indicate differential expression (Padj < 0.05, |FC| ≥ 2) related to injury alone (**d**) or genes with differential injury responses in *Piezo1* mutant versus wild-type mice (**e**).

nature portfolio

Corresponding author(s): Diane Mathis

Last updated by author(s): Jan 11, 2026

Reporting Summary

Nature Portfolio wishes to improve the reproducibility of the work that we publish. This form provides structure for consistency and transparency in reporting. For further information on Nature Portfolio policies, see our Editorial Policies and the Editorial Policy Checklist.

Statistics

For all statistical analyses, confirm that the following items are present in the figure legend, table legend, main text, or Methods section.

n/a	Confirmed
☐	☒ The exact sample size (*n*) for each experimental group/condition, given as a discrete number and unit of measurement
☐	☒ A statement on whether measurements were taken from distinct samples or whether the same sample was measured repeatedly
☐	☒ The statistical test(s) used AND whether they are one- or two-sided *Only common tests should be described solely by name; describe more complex techniques in the Methods section.*
☒	☐ A description of all covariates tested
☐	☒ A description of any assumptions or corrections, such as tests of normality and adjustment for multiple comparisons
☐	☒ A full description of the statistical parameters including central tendency (e.g. means) or other basic estimates (e.g. regression coefficient) AND variation (e.g. standard deviation) or associated estimates of uncertainty (e.g. confidence intervals)
☐	☒ For null hypothesis testing, the test statistic (e.g. *F*, *t*, *r*) with confidence intervals, effect sizes, degrees of freedom and *P* value noted *Give P values as exact values whenever suitable.*
☒	☐ For Bayesian analysis, information on the choice of priors and Markov chain Monte Carlo settings
☒	☐ For hierarchical and complex designs, identification of the appropriate level for tests and full reporting of outcomes
☐	☒ Estimates of effect sizes (e.g. Cohen's *d*, Pearson's *r*), indicating how they were calculated

Our web collection on statistics for biologists contains articles on many of the points above.

Software and code

Policy information about availability of computer code

Data collection	BD FACSDiva (v9.0.1 and v9.4), SpectroFlo (v3.3.0), Bruker BioAFM SPM software (v8)
Data analysis	R (v4.4.3), RStudio (v2024.12.1.563), BiocManager (v1.30.25), tidyverse (v2.0.0), DESeq2 (v1.46.0), apeglm (v1.28.0), dplyr (v1.1.4), plotly (v4.10.4), tidyr (v1.3.1), knitr (v1.5), ggplot2 (v3.5.2), ggrepel (v0.9.6), ggbreak (v0.1.4), devtools (v2.4.5), fgsea (v1.32.0), data.table (v1.17.0), biomarRt (v2.62.1), RColorBrewer (v1.1.3), STAR (v2.7.3a), featureCounts (v2.0.0), RSeQC (v2.6.4), Metascape, FlowJo (v10.10.0), GraphPad Prism (v10.4.1), ImageJ (v1.54g), JPK Data Processing (v8.0.154)

For manuscripts utilizing custom algorithms or software that are central to the research but not yet described in published literature, software must be made available to editors and reviewers. We strongly encourage code deposition in a community repository (e.g. GitHub). See the Nature Portfolio guidelines for submitting code & software for further information.

Data

Policy information about availability of data

All manuscripts must include a data availability statement. This statement should provide the following information, where applicable:

- Accession codes, unique identifiers, or web links for publicly available datasets
- A description of any restrictions on data availability
- For clinical datasets or third party data, please ensure that the statement adheres to our policy

Transcriptomes from RNA-seq of whole skeletal muscles, hearts, liver specimens and sorted MmSCs have been deposited in the Gene Expression Omnibus (GSE297515). Source data are provided with this paper.

Research involving human participants, their data, or biological material

Policy information about studies with human participants or human data. See also policy information about sex, gender (identity/presentation), and sexual orientation and race, ethnicity and racism.

Reporting on sex and gender	N/A
Reporting on race, ethnicity, or other socially relevant groupings	N/A
Population characteristics	N/A
Recruitment	N/A
Ethics oversight	N/A

Note that full information on the approval of the study protocol must also be provided in the manuscript.

Field-specific reporting

Please select the one below that is the best fit for your research. If you are not sure, read the appropriate sections before making your selection.

☒ Life sciences ☐ Behavioural & social sciences ☐ Ecological, evolutionary & environmental sciences

For a reference copy of the document with all sections, see nature.com/documents/nr-reporting-summary-flat.pdf

Life sciences study design

All studies must disclose on these points even when the disclosure is negative.

Sample size	No statistical methods were used to predetermine sample sizes; however, sample sizes were selected based on previous publications in the field (Hanna et al. 2023 Immunity; Yaghi et al. 2023 Nat Immunol; Langston et al. 2023 Sci Immunol) and are indicated in the figure legends.
Data exclusions	As indicated in the Materials and Methods, analyses of bulk RNA-seq data involved upstream quality control steps: samples with <1 million uniquely mapped reads or with fewer than 8000 genes with over 10 reads were excluded from normalization. Additional quality control after normalization included removal of biological replicates with a poor Pearson's correlation (r <0.9). Genes with fewer than 10 reads across samples within any condition were removed. Analysis of data produced by atomic force microscopy on sections of skeletal muscle involved selection uniform rectangular subregions with height profiles within the known thickness of each section (boxed regions in figures). Outlier analysis was performed for each condition across all mice using the ROUT test (GraphPad Prism) with Q value threshold of 0.05.
Replication	Bulk RNA-seq analyses were performed once; all other experiments were performed at least twice.
Randomization	Mice with the same genotypes were randomly assigned to interventions in all cases.
Blinding	Exercise capacity tests were performed blinded. When possible, investigators converted sample identities into numbers after harvesting tissue from mice to temporarily blind them through sample processing and data collection.

Reporting for specific materials, systems and methods

We require information from authors about some types of materials, experimental systems and methods used in many studies. Here, indicate whether each material, system or method listed is relevant to your study. If you are not sure if a list item applies to your research, read the appropriate section before selecting a response.

Materials & experimental systems

n/a	Involved in the study
☐	☒ Antibodies
☒	☐ Eukaryotic cell lines
☒	☐ Palaeontology and archaeology
☐	☒ Animals and other organisms
☒	☐ Clinical data
☒	☐ Dual use research of concern
☒	☐ Plants

Methods

n/a	Involved in the study
☒	☐ ChIP-seq
☐	☒ Flow cytometry
☒	☐ MRI-based neuroimaging

Antibodies

Antibodies used

BioLegend (clone; cat#; dilution factor):
Anti-CD45-BV605 (30-F11; 103139; 200)
Anti-CD45-BV510 (30-F11; 103138; 200)
Anti-CD31-BV605 (MEC13.3; 102427; 200)
Anti-CD31-FITC (MEC13.3; 102506; 200)
Anti-Sca1-PerCP-Cy5.5 (D7; 108124; 200)
Anti-CD140a-APC (APA5; 135908; 200)
Anti-CD140a-PE-Cy7 (APA5; 135911; 200)
Anti-CD54-BV711 (YN1/1.7.4; 116143; 200)
Anti-CD106-PE (429; 105713; 100)
Anti-CD11b-PerCP-Cy5.5 (M1/70; 101228; 200)
Anti-CD11b-PE (M1/70; 101208; 200)
Anti-CD64-BV421 (X54-5/7.1; 139309; 100)
Anti-Ly6G-APC-Cy7 (1A8; 127624; 200)
Anti-Ly6G-BV510 (1A8; 127633; 200)
Anti-Ly6G-AF700 (1A8; 127622; 200)
Anti-Ly6C-BV711 (HK1.4; 128037; 200)
Anti-Ly6C-FITC (HK1.4; 128006; 200)
Anti-MHCII-FITC (M5/114.15.2; 107606; 200)
Anti-SiglecF-PE (S17007L; 155505; 200)
Anti-SiglecF-AF700 (S17007L; 155533; 200)
Anti-CD4-BV711 (GK1.5; 100447; 200)
Anti-CD4-BV785 (GK1.5; 100453; 200)
Anti-CD8-AF700 (53-6.7; 100730; 200)
Anti-Helios-Pacific Blue (22F6; 137220; 100)
Anti-CCL2-PE (2H5; 505903; 100)
Anti-IL-6-APC (MP5-20F3; 504507; 100)

Invitrogen (clone; cat#):
Anti-TCRbeta-BUV737 (H57-597; 367-5961-82; 200)

Novus Biologicals (clone; cat#):
Anti-TNC-AF647 (4C8MS; NB110-68136AF647; 300)

BD Pharmingen (clone; cat#):
Anti-Ki67-AF700 (16A8; 652420; 100)

eBioscience (clone; cat#):
Anti-Foxp3-APC (FJK-16s; 17-5773-82; 200)
Anti-ST2-PE-Cy7 (RMST2-2; 25-9335-82; 200)
Anti-RORgamma-PE (AFKJS-9; 12-6988-82; 50)

Validation

All antibodies used in this study are commercially available and were validated by the respective manufacturer. Validation statements are available online on each manufacturer's website.

Animals and other research organisms

Policy information about studies involving animals; ARRIVE guidelines recommended for reporting animal research, and Sex and Gender in Research

Laboratory animals

All mice were maintained under SPF conditions at Harvard Medical School (HMS) facilities in accordance with Institutional Animal Care and Use Committee guidelines (IS00001257 and IS00001725). The animal room was on a 24h light/dark cycle (lights on at 06:00 and off at 18:00) and ambient temperature and humidity were 72°F and 52%. C57BL/6J, C57BL/6-Tg(Pdgfra-cre)1Clc/J (PDGFRa-Cre), and B6.Cg-Piezo1tm2.1Apat/J (Piezo1f) mice were originally purchased from Jackson Laboratory, and mice were bred and maintained in-house before use in experiments between 8-10 weeks of age. All experiments using these strains were conducted with littermate

	controls. Aged mice were imported from the National Institute on Aging (NIA) aged rodent colony, which is maintained at Charles River Laboratories by the Translational Research Branch within the NIA Division of Aging Biology, at least 2 weeks prior to use for experiments.
Wild animals	No wild animals were used in this study.
Reporting on sex	For cytofluorometric analyses and performance assays using Pdgfra-Cre.Piezo1f/f and Pdgfra-Cre.Piezo1+/+ littermates, both male and female mice were included in pilot experiments; no sex dimorphism was observed. Hence, data from both sexes were combined. Only male mice were used for all other experiments and assays.
Field-collected samples	No field-collected samples were in this study.
Ethics oversight	Experiments were conducted under protocols approved by Harvard Medical School's Institutional Animal Care and Use Committee.

Note that full information on the approval of the study protocol must also be provided in the manuscript.

Plants

Seed stocks	N/A
Novel plant genotypes	N/A
Authentication	N/A

Flow Cytometry

Plots

Confirm that:

☐ The axis labels state the marker and fluorochrome used (e.g. CD4-FITC).

☒ The axis scales are clearly visible. Include numbers along axes only for bottom left plot of group (a 'group' is an analysis of identical markers).

☐ All plots are contour plots with outliers or pseudocolor plots.

☒ A numerical value for number of cells or percentage (with statistics) is provided.

Methodology

Sample preparation	Cells were isolated from mouse skeletal muscle as described in the methods.
Instrument	Samples were acquired on a FACSymphony A5 flow cytometer (BD Biosciences) or Aurora spectral flow cytometer (Cytek); sorting was performed on a FACSAria (BD Biosciences).
Software	Data were collected using BD FACSDiva (v9.0.1 and v9.4) and SpectroFlo (v3.3.0) software and analyzed using FlowJo software.
Cell population abundance	Sorting purity was 95-99% based on post-sort cytofluorometric verification.
Gating strategy	Representative gating strategies for all sorting and immunophenotyping are included (Extended data 1a, 4a, 4g, 5c, 6a, 6b).

☒ Tick this box to confirm that a figure exemplifying the gating strategy is provided in the Supplementary Information.